Global Ionospheric and Thermospheric Effects of the June 2015 Geomagnetic Disturbances

Multi-Instrumental Observations and Modeling

Astafyeva, E; Zakharenkova, I; Huba, J. D.; Doornbos, E.; van den Ijssel, J.

DOI
10.1002/2017JA024174

Publication date
2017

Document Version
Final published version

Published in
Journal Of Geophysical Research-Space Physics

Citation (APA)
Astafyeva, E., Zakharenkova, I., Huba, J. D., Doornbos, E., & van den Ijssel, J. (2017). Global Ionospheric and Thermospheric Effects of the June 2015 Geomagnetic Disturbances: Multi-Instrumental Observations and Modeling. *Journal Of Geophysical Research-Space Physics*, *122*(11), 11716–11742 . https://doi.org/10.1002/2017JA024174

AGU PUBLICATIONS

JGR

Journal of Geophysical Research: Space Physics

RESEARCH ARTICLE
10.1002/2017JA024174

Key Points:
- We analyze global ionospheric/thermospheric effects of geomagnetic disturbances (substorms and major storm) occurred on 22-23 June 2015
- The storm caused quite significant effects in the ionosphere and thermosphere on both dayside and nightside
- SAMI3/RCM model shows rather good agreement with observations at the first stage of the storm, but less agreement is found at the end of the storm

Supporting Information:
- Supporting Information S1
- Figure S1
- Figure S2
- Animation S1
- Animation S2

Correspondence to:
E. Astafyeva,
astafyeva@ipgp.fr

Citation:
Astafyeva, E., Zakharenkova, I., Huba, J. D., Doornbos, E., & van den IJssel, J. (2017). Global Ionospheric and thermospheric effects of the June 2015 geomagnetic disturbances: Multi-instrumental observations and modeling. *Journal of Geophysical Research: Space Physics*, *122*, 11,716–11,742. https://doi.org/10.1002/2017JA024174

Received 27 MAR 2017
Accepted 21 OCT 2017
Accepted article online 26 OCT 2017
Published online 20 NOV 2017

Global Ionospheric and Thermospheric Effects of the June 2015 Geomagnetic Disturbances: Multi-Instrumental Observations and Modeling

E. Astafyeva[1], I. Zakharenkova[1], J. D. Huba[2], E. Doornbos[3], and J. van den IJssel[3]

[1]Department of Planetology and Space Sciences, Institut de Physique du Globe de Paris, Paris Sorbonne Cité, University of Paris Diderot, Paris, France, [2]Plasma Physics Division, Naval Research Laboratory, Washington, DC, USA, [3]Department of Space Engineering, Delft University of Technology, Delft, Netherlands

Abstract By using data from multiple instruments, we investigate ionospheric/thermospheric behavior during the period from 21 to 23 June 2015, when three interplanetary shocks (IS) of different intensities arrived at Earth. The first IS was registered at 16:45 UT on 21 June and caused ~50 nT increase in the *SYM-H* index. The second IS arrived at 5:45 UT on 22 June and induced an enhancement of the auroral/substorm activity that led to rapid increase of thermospheric neutral mass density and ionospheric vertical total electron content at high latitudes. Several hours later, topside electron content and electron density increased at low latitudes on the nightside. The third and much larger IS arrived at 18:30 UT on 22 June and initiated a major geomagnetic storm that lasted for many hours. The storm provoked significant effects in the thermosphere and ionosphere on both dayside and nightside. In the thermosphere, the dayside neutral mass density exceeded the quiet time levels by 300–500%, with stronger effects in the summer hemisphere. In the ionosphere, both positive and negative storm effects were observed on both dayside and nightside. We compared the ionospheric observations with simulations by the coupled Sami3 is Also a Model of the Ionosphere/Rice Convection Model (SAMI3/RCM) model. We find rather good agreement between the data and the model for the first phase of the storm, when the prompt penetration electric field (PPEF) was the principal driver. At the end of the storm main phase, when the ionospheric effects were, most likely, driven by a combination of PPEF and thermospheric winds, the modeling results agree less with the observations.

1. Introduction

It is known that the Earth's ionosphere can change the path of radio signals and that steep density gradients can cause severe radio scintillations and losses of lock (e.g., Afraimovich et al., 2011; Astafyeva et al., 2014; Basu et al., 2008; Kelly et al., 2014). Therefore, nowadays, an extensive study of the ionospheric "weather" and its forecast based on correct modeling becomes of high priority and importance.

Ionospheric disturbances can be caused by many geophysical phenomena (e.g., solar flares, geomagnetic storms, stratospheric warmings, large earthquakes, etc.) and by man-made events (e.g., rocket launches, explosions, nuclear tests). The disturbances, either plasma density increases or decreases, can occur during both geomagnetically quiet and disturbed conditions; however, the most significant ionospheric alterations are provoked by geomagnetic storms, when the ionosphere is perturbed strongly and globally.

Study of ionospheric effects of geomagnetic storms (ionospheric storms) remains, so far, one of the most difficult tasks of the ionosphere physics. The main challenge in our understanding of the ionospheric storms is in the fact that the storm time ionospheric behavior is controlled by several competing dynamical and electrodynamical processes, such as penetration of electric fields of magnetospheric origin (also referred to as prompt penetration electric fields, PPEF), the disturbance dynamo electric fields, and the interaction between ions and neutrals.

Recent development of networks of ground-based instruments and launch of new satellite missions allowed to reveal new aspects of the development of ionospheric and thermospheric storms with unprecedented details (e.g., Afraimovich et al., 2013; Astafyeva et al., 2016; Balan et al., 2012, 2011; Foster & Coster, 2007; Foster & Rideout, 2005; Lei et al., 2008, 2014; Liu & Lühr, 2005; Nayak et al., 2016; Tsugawa et al., 2003; Zhong et al., 2016). However, the ionospheric storms remain complex phenomena and, despite numerous efforts, are not well forecasted yet.

The main aim of this study is to present a detailed multi-instrumental global overview of ionospheric and thermospheric behavior during the period of time from 21 to 23 June 2015, which includes the quiet time period and the arrival of three interplanetary shocks (IS) of different intensities. Of these three IS, the third and the largest one was followed by a coronal mass ejection that provoked a major geomagnetic storm with the minimum of the *SYM-H* index excursion of −207 nT. Astafyeva et al. (2016) made the first preliminary analysis of the ionospheric response during the main phase of this major storm that occurred on 22–23 June 2015. By using measurements of the in situ electron density and the vertical electron content over the three Swarm satellites, they found strong effects of both positive and negative ionospheric storms during the main phase of this geomagnetic storm. Analysis of the equatorial electrojet (EEJ) data from the magnetic Swarm observations and of the variations of ionospheric parameters led to conclusion that the PPEF appeared to be the main driver of the observed ionospheric effects in the topside ionosphere at the beginning of the main phase of the storm. In this work, we make more profound investigation of both ionospheric and thermospheric alterations during the extended time period on the global scale; in addition to the Swarm constellation results, we use vertical total electron content (VTEC) maps from ground-based Global Navigation Satellite Systems (GNSS) receivers, and we further compare our ionospheric observations with the Naval Research Laboratory SAMI3 (Sami3 is Also a Model of the Ionosphere) coupled with the Rice Convection Model (RCM) simulation results.

2. Data Set: Observations and Modeling

2.1. Observations: Instrument Set

The observational part of our study contains measurements (1) from ground-based GNSS receivers and (2) from the Swarm constellation.

From data of dual-frequency GNSS receivers it is possible to calculate the absolute vertical total electron content (VTEC). Global maps of GPS-derived VTEC have been widely used for ionospheric studies for nearly three decades (e.g., Afraimovich et al., 2013; Astafyeva et al., 2007; Foster & Coster, 2007; Foster & Rideout, 2005; Liu et al., 2006, 2014; Mannucci et al., 1998; Tsugawa et al., 2003; Verkhoglyadova et al., 2013). More recently, in addition to the GPS data, it has been proposed to use Global Navigation Satellite System (GLONASS) measurements to estimate the VTEC (Zakharenkova et al., 2016). In this paper, we use the same technique as Zakharenkova et al. (2016), and we plot global VTEC maps for the period from 21 to 23 June 2015. In addition to that, we also calculate the storm time residuals with respect to quiet time values of 20 June 2015.

Swarm is a recent satellite mission of the European Space Agency (ESA). Three identical spacecraft, Alpha (A), Bravo (B), and Charlie (C), were launched on 22 November 2013 and are to study the Earth's magnetic field and the near-space environment (e.g., Olsen et al., 2013). Each of the Swarm spacecraft carries onboard scalar and fluxgate magnetometers, GPS receiver, Langmuir Probe, accelerometer, plasma, and electric field instruments. The Swarm satellites have a polar orbit with 87–88° of inclination. Swarm A and C fly side by side at the altitude of ~460 km, while the orbital altitude of Swarm B (SWB) is ~530 km. In June 2015, the tandem satellites A and C crossed the equator at ~11 and ~23 LT, and Swarm B did it at ~13 and ~01 LT. Because Swarm A and C provide similar results, here we shall only show Swarm C (SWC) data.

To study the ionospheric behavior during the June 2015 magnetic disturbances, we analyze variations of the electron density from the Langmuir probes and those of VTEC above the satellites (i.e., in the topside part of the ionosphere). A detailed description of the technique to calculate VTEC from a space borne GPS receiver can be found in our previous works (e.g., Astafyeva, Zakharenkova & Doornbos, 2015; Zakharenkova & Astafyeva, 2015). To distinguish the topside VTEC estimated above the satellites from the "total" VTEC derived from ground-based GNSS receivers, below we refer to the topside vertical electron content as topside vertical electron content (VEC) or VEC.

The thermospheric behavior during the considered period of time is investigated by the first-time use of a new data set of the neutral mass density that is derived using data from the GPS receivers on board the Swarm satellites. It is known that the positioning information provided by GPS receivers can be used to accurately estimate nongravitational forces acting on the spacecraft, such as aerodynamic drag, when all other forces are accurately modeled in the orbit determination process (van den IJssel, 2014; van den IJssel & Visser, 2007). Space accelerometers measure the forces directly, at much finer temporal resolution than the GPS receivers, but GPS receiver data have always been required to calibrate the measurements at long

temporal scales. Unfortunately, the accelerometer measurements on Swarm suffer from a variety of disturbances, the most prominent being very strong temperature-induced bias variations and frequent sudden bias changes (Siemes et al., 2016). Only data from Swarm C are partly available. In this work we use the new data set of GPS-derived thermosphere densities, which is available for all three Swarm satellites. The densities are derived from accelerations estimated in an orbit determination using a Kalman filter approach, resulting in a smoothed representation of the true accelerations. Contrary to the accelerometer data, the density data therefore do not represent density variations with spatial scales below about 5,000 km along the satellite tracks and cannot be used to identify localized density variations and identify traveling disturbances. As we will show in this paper, the data are of good use to study effects of storms in the thermosphere on a global level and to identify differences in the response between the local time sectors, latitude sectors, and altitudes sampled by the three Swarm satellites.

2.2. Modeling: SAMI3/RCM-Simulated VTEC, Topside VEC, and Ne

The models used in this study are the Naval Research Laboratory (NRL) ionosphere-plasmasphere model SAMI3 (Huba & Joyce, 2010; Huba et al., 2000) and the Rice Convection Model (RCM) (Sazykin et al., 2002; Toffoletto et al., 2003; Wolf et al., 1991). SAMI3 models the cold plasma ionosphere/plasmasphere system, while RCM models the inner magnetosphere including the ring current. In SAMI3/RCM, the models are coupled electrodynamically through the electrostatic potential Φ (Huba et al., 2005, 2016; Huba & Sazykin, 2014). SAMI3 calculates the electric field from the neutral wind dynamo and provides the solar EUV ionospheric conductance to RCM to calculate the electric field driven by the high-latitude currents. This self-consistent electric field is used by both SAMI3 and RCM to transport the plasma due to the E × B drift.

In this work, the SAMI3/RCM was run for 5 days: 19–23 June 2015. The geophysical parameters used in SAMI3/RCM are the following: 19 June 2015 (day = 170, $F_{10.7}$ = 141.8, $F_{10.7}$A = 120.6, and Ap = 6), 20 June 2015 (day = 171, $F_{10.7}$ = 139.8, $F_{10.7}$A = 119.9, and Ap = 3), 21 June 2015 (day = 172, $F_{10.7}$ = 136.0, $F_{10.7}$A = 118.4, and Ap = 1), 22 June 2015 (day = 173, $F_{10.7}$ = 255.0, $F_{10.7}$A = 118.4, and Ap = 7), and 23 June 2015 (day = 174, $F_{10.7}$ = 119.9, $F_{10.7}$A = 117.7, and Ap = 57). The SAMI3 grid is [*nz*; *nf*; *nl*] = [204,124,96], where *nz* is the number of cells along a magnetic field line, *nf* is the number of «magnetic field lines», and *nl* is the number of longitudes. The SAMI3 grid extends to ±89°. The RCM uses the Hilmer-Voigt time-dependent magnetic field model (Hilmer & Voigt, 1995) and a time-varying potential on the high-latitude boundary, both estimated to vary throughout the storm interval using the NASA OMNI 5 min resolution history of solar wind and interplanetary magnetic field (IMF) parameters, as well as the *SYM-H* index (shown in Figure 1). The Weimer model is used for the high-latitude potential for the region above the RCM upper boundary. Both SAMI3 and RCM use a centered, aligned dipole magnetic field in the ionosphere. However, we map the simulation results to the International Geographic Reference Field (IGRF) using the Richmond apex model (Richmond, 1995) in order to better compare the model results with observations. For the neutral composition and temperature, SAMI3 uses the empirical model NRLMSISE00 (Picone et al., 2002), and for the neutral wind HWM14 (Drob et al., 2015) is used. Lastly, the Flare Irradiance Spectral Model (FISM) (Chamberlin et al., 2007) is used by SAMI3 to specify the EUV spectra to calculate the photoionization rate.

The simulation results we present here are (1) the total VTEC estimated between the ground and the altitude of the GNSS satellites, (2) the topside VEC calculated from the Swarm B and C altitudes (i.e., 530 km and 460 km, respectively) to the GPS satellite altitude (~20,000 km), and (3) the electron density Ne at the Swarm B and C altitudes.

3. Geomagnetic Disturbances on 21–23 June 2015: Solar Wind, Interplanetary, and Geophysical Parameters

Figure 1 shows variations of solar wind, interplanetary, and geophysical parameters during the period of time from 20 to 23 June 2015. One can see that the day of 20 June was geomagnetically quiet day; therefore, in our work, the data for this day will be used as a quiet time reference values. To study the June 2015 disturbance effects on the ionosphere and thermosphere, we analyze 3 day period of time from 21 to 23 June, when three IS arrived at Earth. Originated from the Sun's active region 2371, these IS were associated with coronal mass ejections (CME) (Liu et al., 2015). The first two IS arrivals that were observed at 16:45 UT on 21 June and at 05:45 UT on 22 June were associated with halo and partial halo CME caused by filament eruptions on 18 and 19 June. The third and much larger IS that arrived at 18:38 UT on 22 June was associated with a full

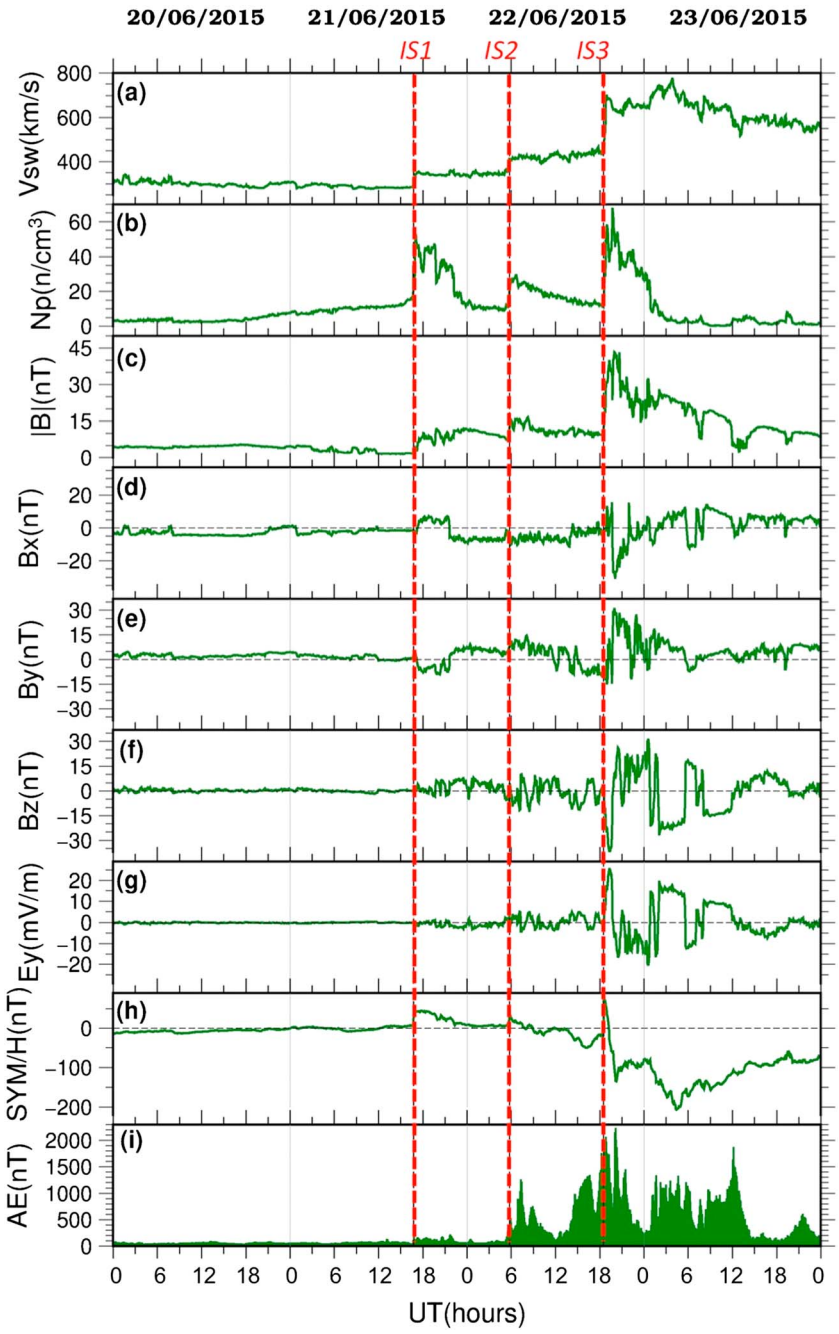

Figure 1. Variations of solar wind, interplanetary, and geomagnetic parameters on 20–23 June 2015: (a) solar wind speed V_{sw}, (b) proton density Np, (c) plasma beta parameter, (d) interplanetary magnetic field (IMF) B_x component, (e) the IMF B_y component, in GSM coordinates (in green), and the IMF averaged magnitude |B| (in black), (f) the IMF B_z component (GSM), (g) interplanetary electric field (IEF) E_y component, calculated as $-B_z \times V_{sw}$, (h) geophysical *SYM-H* index, and (i) the auroral electrojet (*AE*) index. All the data are 5 min averaged and are available from the OMNIWeb data services (http://omniweb.gsfc.nasa.gov). The dates are shown on the top of the figure; the time of arrivals of the three interplanetary shocks (IS) is indicated by red vertical dashed lines and marked as IS1, IS2, and IS3, respectively, on the top of the upper panel. Thin gray vertical lines mark the 24 UT timelines.

halo giant CME that erupted during a double-peak M2 flare on 21 June. Figure 1 demonstrates that all of the three IS events were accompanied by abrupt changes in the solar wind speed and density and in the amplitude of the interplanetary magnetic field (IMF) B_x, B_y, and B_z components. One can see that the third event was especially strong.

These three IS with different solar wind and IMF parameters caused different effects on Earth. As known, the main cause of geomagnetic disturbances (substorms and storms) is the southward directed IMF B_z component, which causes the reconnection with the Earth's magnetic field lines. Besides the IMF B_z component, the solar wind speed and density are known to play an important role in the strength of an IS impact (Gonzalez et al., 1994). Figure 1 shows that at the arrival of the first IS event the solar wind density sharply changed from 10 to 50 n/cm^3, and the solar wind speed changed from 300 to ~400 km/s. This compressed the magnetosphere and caused ~40 nT sudden increase in the *SYM-H* index, which lasted for the next 4.5 h (Figure 1h). However, the IMF B_z component remained positive, so that no substorm activity followed, as seen in the auroral electrojet (*AE*) index behavior during this period of time (Figure 1i).

The second IS was accompanied by a smaller jump in the solar wind density, and it provoked a small short-term 20–27 nT increase in the *SYM-H* index (Figure 1h). The IMF B_z turned southward with the arrival of the IS2, which caused an enhancement in the auroral activity (Figure 1i). From ~14 UT on 22 June the *AE* index experienced a second strong enhancement that lasted until ~17:30 UT. The effect of this enhanced substorm activity can be seen in the decrease of the *SYM-H* index down to ~−40 nT (Figure 1h).

Unlike the two previous events, the arrival of the third IS was followed by a giant CME at 18:38 UT on 22 June. The CME was accompanied by significant jumps in the solar wind speed V_{sw} from ~450 km/s to ~700 km/s (Figure 1a), and in the density Np from 10 to 58 n/cm^3 (Figure 1b). This CME caused significant changes in the IMF (Figures 1c–1f), and it provoked a ~77 nT increase in the *SYM-H* index (Figure 1h). At the IS3 arrival, the IMF B_z component was intense and directed southward (Figure 1f), which led to magnetic reconnection and to a development of a strong geomagnetic storm, with the minimum of *SYM-H* index value of −207 nT (reached at ~05:30 UT on 23 June, Figure 1h). In terms of variations of the *SYM-H* index, this storm is the second largest storm in the 24th solar cycle.

One of the main features of this storm is multiple large-amplitude fluctuations of the IMF B_z during the main and the recovery phases (Figure 1f). The IMF B_z was first largely negative (southward) from 18:38 to 20 UT with the minimum of −37.6 nT at ~19:20 UT, which is the most negative excursion measured in 2015 then turned positive (northward) for ~1.5 h with the maximum of ~26.3 nT reached by 20:30 UT. From ~20:55 UT to 21:15 UT the IMF B_z was directed southward, and from ~21:25 UT the IMF B_z turned northward and remained that until 00:50 UT of the next day. Between 00:55 and 1.8 UT there occurred rapid small-amplitude fluctuations of the IMF B_z, and from ~01:55 UT the B_z component went sharply down to −27 nT and persisted intensively negative until 05:30 UT. The IMF B_z oscillations continued even until ~12 UT, that is, during the recovery phase, that started at ~4:30 UT, as seen from the *SYM-H* behavior in Figure 1h. Following such IMF B_z oscillations, the interplanetary electric field (IEF) E_y component, that is usually calculated from the MHD approximation as $-V_{sw} \times B_z$ (http://omniweb.gsfc.nasa.gov), varied between −15 and +20 mV/m during this storm (Figure 1g). It should be noted that such E_y amplitude is comparable with superstorm values (e.g., Fejer et al., 2007; Huang et al., 2005; Verkhoglyadova et al., 2008).

The June 2015 storm was also characterized by enhanced substorm activity. The *AE* index reached ~2,300 nT at the beginning of the main phase of the storm (Figure 1i). The *AE* further grew during next long-time southward B_z turns from ~01:55 UT to 05:30 UT and from ~8 UT to 12 UT.

4. Global Ionospheric VTEC Behavior During 21–23 June 2015: Observations and Modeling

4.1. Global Maps of VTEC as Derived From GNSS Receivers

Animation S1 (supporting information) presents the global maps of VTEC as calculated from both GPS and GLONASS measurements for the period of time from 21 to 23 June 2015 (upper left panel). Animation S2 (supporting information) shows the global maps of VTEC deviations with respect to the quiet time VTEC values of 20 June 2015.

One can see that on 21 June 2015 and before the arrival of the IS3 on 22 June 2015, the absolute VTEC did not exceed 5–8 total electron content unit, 1 TECU = 10^{16} el m^{-2} (TECU) on the nightside and at high latitudes on the dayside, and the maximum VTEC values 50–60 TECU were reached at low latitude and midlatitude on the dayside. During this geomagnetically quiet time period, the deviation VTEC (dVTEC) varied within ±10–15 TECU throughout the globe, except for the local increased ionization spot up to 20 TECU in the

Asian region at ~8–10 UT on 21 June (i.e., local presunset sector). About 20 TECU dVTEC increase can be seen on 22 June from 6 to 9 UT over the Asian region, and smaller dVTEC increase of ~10 TECU can be seen in Europe and North Africa. From 16 to 18 UT, one can observe ~15–20 TECU increase over South America. The time of occurrence of these enhancements corresponds to the time development of the two substorms, as seen in Figure 1i.

With the beginning of the geomagnetic storm at 18:38 UT on 22 June strong storm time effects occurred. First, the VTEC sharply increased at high latitudes of the Southern Hemisphere (SH) and it continued to grow up within next several hours. Second, the middle- and low-latitude VTEC gradually but largely increased on the dayside, especially high VTEC values were observed over south and northeast of North American continent at 19:30–22:30 UT. The absolute VTEC reached 72 TECU (more than +35 TECU increase on the deviation maps). Other spots of the increased VTEC up to 65–70 TECU (up to +30 + 35 TECU on the deviation maps) can be seen over South America and over the northwest coast of Africa. Note that the low-latitude and high- to middle-latitude increases are, most likely, of different physical mechanisms. They both occur at the beginning of the storm; however, the low-latitude increase disappears shortly after the IMF B_z turns northward, while the increases at middle and partly high latitudes remain for longer time. The spot over North Africa and south Europe first occurred during local evening and presunset hours. With time, the VTEC lowered but remained increased within this area until ~23:00–23:45 UT, that is, even after the sunset and during local premidnight time. This VTEC enhancement disappeared only by ~01:00–02:00 UT of 23 June. Overall, by ~00:45–01:45 UT, the global VTEC drastically decreased on both dayside and nightside of the Earth. From ~02:00 UT, the dayside VTEC started to increase again, and by 05:15–05:45 UT it significantly increased around the local noontime at low latitude and midlatitude. The absolute VTEC reached 70–72 TECU (more than +35 TECU on the deviation maps) over North Australia and Indonesia. At the same time, the absolute VTEC values on the nightside and in the local morning sector went down to ~1–2 TECU, and the VTEC over northern Europe and over the north of Northern America was quite low as well. In terms of the VTEC deviations, the negative storm over the Europe was quite intensive with dVTEC going by −30 TECU below the quiet time values. The positive storm ended shortly after the IMF B_z turned positive at ~5:50 UT. The negative storm effect over Europe continued within next several hours, and by 08:20–08:40 UT the VTEC throughout the globe and especially over the Americas went down to minimum values of several TECU on the nightside and ~30–40 TECU on the dayside.

From ~12:00 UT on 23 June, the dayside low-latitude VTEC increased up to ~40–45 TECU (+15 TECU increase with respect to the quiet time values) over African and Indian sectors. However, we do not observe a dayside VTEC enhancement in the American region with the arrival of the new day. From 15:20 to 19:40 UT, both dayside and nightside show very low VTEC values, not exceeding ~20 TECU. Strong negative storm effects can be seen over the American and European regions until the end of the day of 23 June 2015.

Below we compare these ground-based GNSS measurements with SAMI3/RCM results.

4.2. Global VTEC Maps as Computed by the SAMI3/RCM Model

Global maps of VTEC between 0 and 20,000 km as modeled by the SAMI3/RCM coupled model are shown in Animation S1 (right panel). The corresponding deviation maps of the modeled dVTEC are presented in Animation S2 (right panel).

On 21 June 2015, the quiet time dayside modeled VTEC at low latitudes reached ~50–60 TECU, on the nightside reached 20–30 TECU at low latitudes, which is somewhat overestimated as compared to the observations. At middle and high latitudes we find better agreement with the GNSS-derived VTEC. In reference dVTEC maps, the SAMI3/RCM model predicts almost no deviations from the quiet time levels on 21 June 2015, until the arrival of the IS1, when the dVTEC increases ~7–8 TECU at high latitudes of Northern Hemisphere (NH). This is because the geophysical conditions were very similar for 20 and 21 June 2015.

The arrival of the IS2 at 5:45 UT on 22 June was marked by small-amplitude perturbations at high latitudes in the vicinity of the magnetic poles. At low latitudes on the dayside the dVTEC experienced +15 TECU increase that lasted until ~10 UT (Animation S2, right panel). Similar dVTEC perturbations are later seen at 14:30–18 UT, which is the period of the second substorm that occurred right before the arrival of the IS3. These results are somewhat similar but not identic to the observations.

With the beginning of the geomagnetic storm at 18:38 UT on 22 June, the area of the storm time increased VTEC extended throughout all latitudes on the dayside. At high latitudes, the increase is especially strong in the NH in the American region, as we see a tongue of ionization of ~40–45 TECU over the north of North America (Animations S1 and S2). Another spot of enhanced ionization can be seen at high latitudes around the southern magnetic pole. At low latitude and midlatitude, the maximum of the absolute VTEC reached 72 TECU, which is ~35 TECU more than during quiet time. These simulation results are in ~70% agreement with observations. Overall, the dayside VTEC in the SAMI3/RCM model is larger than that observed, in part because of the very large value of $F_{10.7}$ on 22 June 2015. From ~22:30–24 UT, the dayside VTEC started to diminish and the spot moved back to low latitudes but did not decrease drastically as we observe in the GNSS data.

The VTEC behavior from ~2 to ~6 UT over Australia (local afternoon) and over Atlantic Ocean and South America (local midnight) is the largest discrepancy between the data and the model. While the observations show quite significant positive storm in Asian sector (mostly over Australia and around the equator), the SAMI3/RCM model shows ~−15 TECU decrease in the dayside dVTEC over the magnetic equator (local prenoon time) and no significant storm time changes over Australia. We note that we see an enhancement over the Asian and Pacific regions in absolute modeled VTEC, but not in the dVTEC, which is contrary to the observations (Animation S2).

At the same time, the nightside simulation results showed a significant VTEC decrease over the magnetic equator with concurrent VTEC increase up to ~35 TECU at ~±15° of latitude from the equator. These results, most likely, represent the development and reinforcement of the equatorial ionization anomaly (EIA). It should be noted that occurrence of such effect on the nightside is rare and is usually linked with enhanced electric fields due to the PPEF. However, between 2 and 10 UT on 23 June, the IMF B_z changed the polarity several times. We therefore consider that this effect in the simulation results was due to the action of longer-lived disturbance dynamo, which implies eastward electric fields on the nightside and westward electric fields on the dayside, and leads to reinforcement of the EIA on the nightside and negative storm at low latitudes on the dayside (seen over the Indian Ocean).

One feature was reproduced quite well by the SAMI3/RCM model: ~−20 TECU decrease over Eurasia (high latitude and midlatitude) occurred at 2–6 UT, which is very similar to the observations (Animation S2).

From ~13:30 UT on 23 June, the VTEC lowered throughout the globe, reaching the maximum of only ~38–40 TECU at low latitudes on the dayside. Such VTEC behavior continued until the end of the day.

Thus, we conclude that the SAMI3/RCM reproduced rather well the storm time behavior of the VTEC between 0 and 20,000 km during the first positive phase of the storm. For the second part of the storm, much less agreement is found.

5. Topside Ionosphere Behavior on 21–23 June 2015: Observations and Modeling

5.1. Ionospheric Swarm Observations in the Daytime Sector

Figure 2a shows variations of the VEC above the Swarm B satellite (i.e., above 530 km) during daytime passes (13 LT) for the period of time from 21 to 23 June 2015. The quiet time topside VEC values for the day of 20 June 2015 can be found in Figure S1 (supporting information). The deviation dVEC as compared to the quiet time VEC is shown in Figure 3a.

One can see that on 21 June the topside VEC along satellite profile exhibited a north-south asymmetry, with VEC up to ~9 TECU in NH and around 1–2 TECU in the SH. At the magnetic equator, the VEC above SWB reached ~12–16 TECU. One can also see the quiet time variability of ±5 TECU at low latitudes (Figures 2a and 3a). At high latitudes, the dVEC increase of ~2–5 TECU in both hemispheres was observed after the arrival of the IS2 (tracks 20–22, Figure 3a). At the same time, the low-latitude VEC seemed to decrease by several units; however, it is difficult to attribute this decrease to the substorm as similar low-latitude VTEC behavior is observed on 21 June.

The beginning of the storm at ~18:38 UT on 22 June 2015 changed the topside VEC behavior drastically at all latitudes. The equatorial VEC increased first up to 28–30 TECU, and by ~22:30 UT it reached 36 TECU (Figure 2a), which is more than 10 TECU more than during quiet time period (Figure 3a). During this first

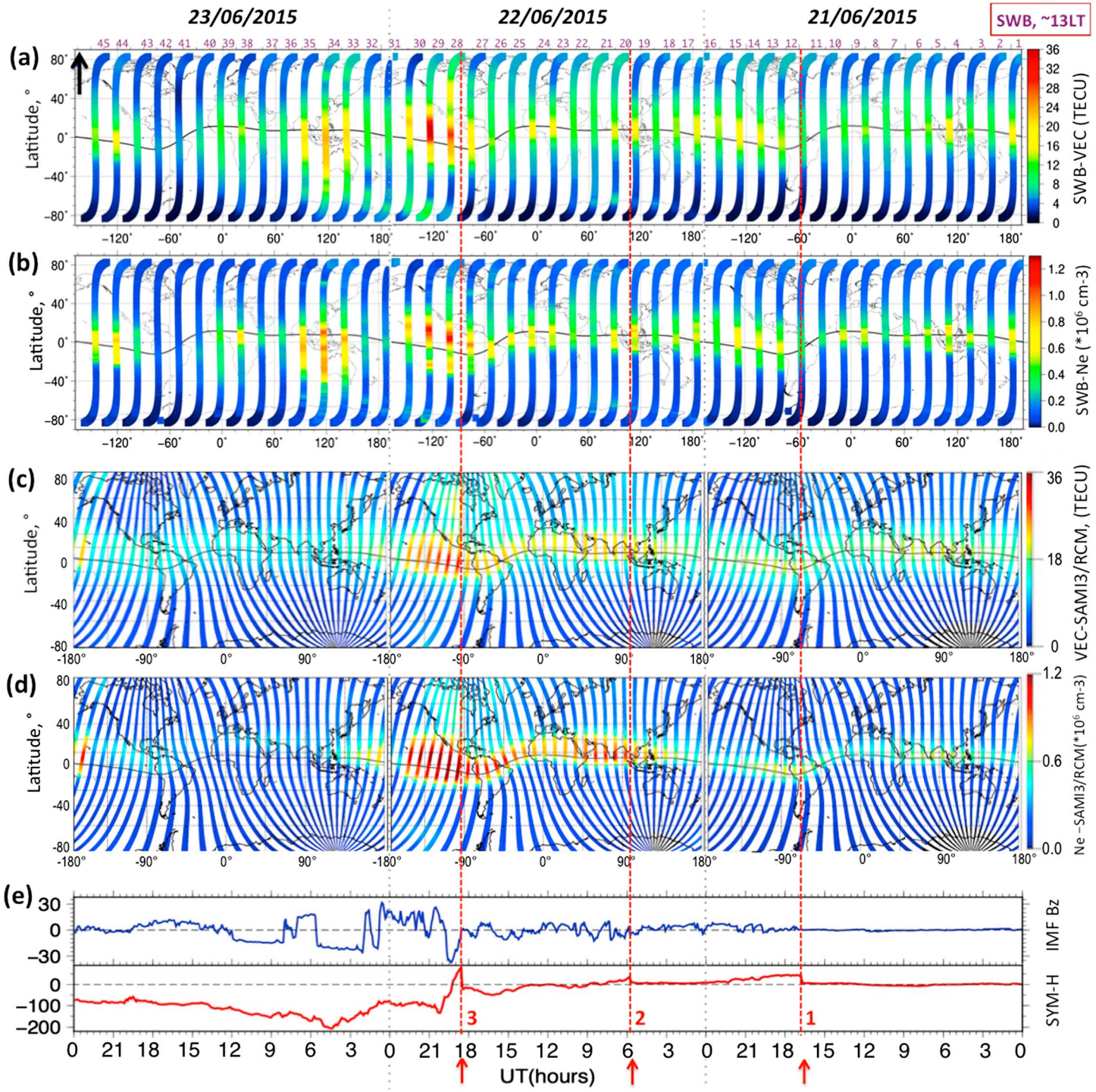

Figure 2. Ionospheric measurements by Swarm B (SWB) satellite during the daytime passes (equatorial crossing at ~13 LT) on 21–23 June 2015: (a) variations of the topside VEC above the Swarm B satellite altitude of ~530 km as calculated from GPS receiver on board the satellite and (b) in situ electron density Ne as measured by the Langmuir Probe on board SWB. Color shows the amplitude of the VEC (Figure 2a), the Ne (Figure 2b), and the corresponding color scales are shown on the right side of the panels. Violet numbers on the top show satellite track number. Black arrow in the top left panel shows the direction of the satellite movement, ascending or descending; SAMI3/RCM model-simulated VEC above (c) 530 km and the electron density Ne at the altitude of (d) 530 km for the time period 21–23 June 2015. The presented tracks are the SAMI3/RCM simulations for the time and longitude at the equatorial crossings of the SWB satellite presented in Figures 2a and 2b; (e) variations of the IMF B_z component (blue curve) and *SYM-H* index (red curve) on 21–23 June 2015. The dates are shown on the top of the figure, and the universal time (UT, running from right to left) is shown on the bottom. Red arrows and vertical red dashed lines indicate the time of arrivals of the three IS. The coordinates are geographic.

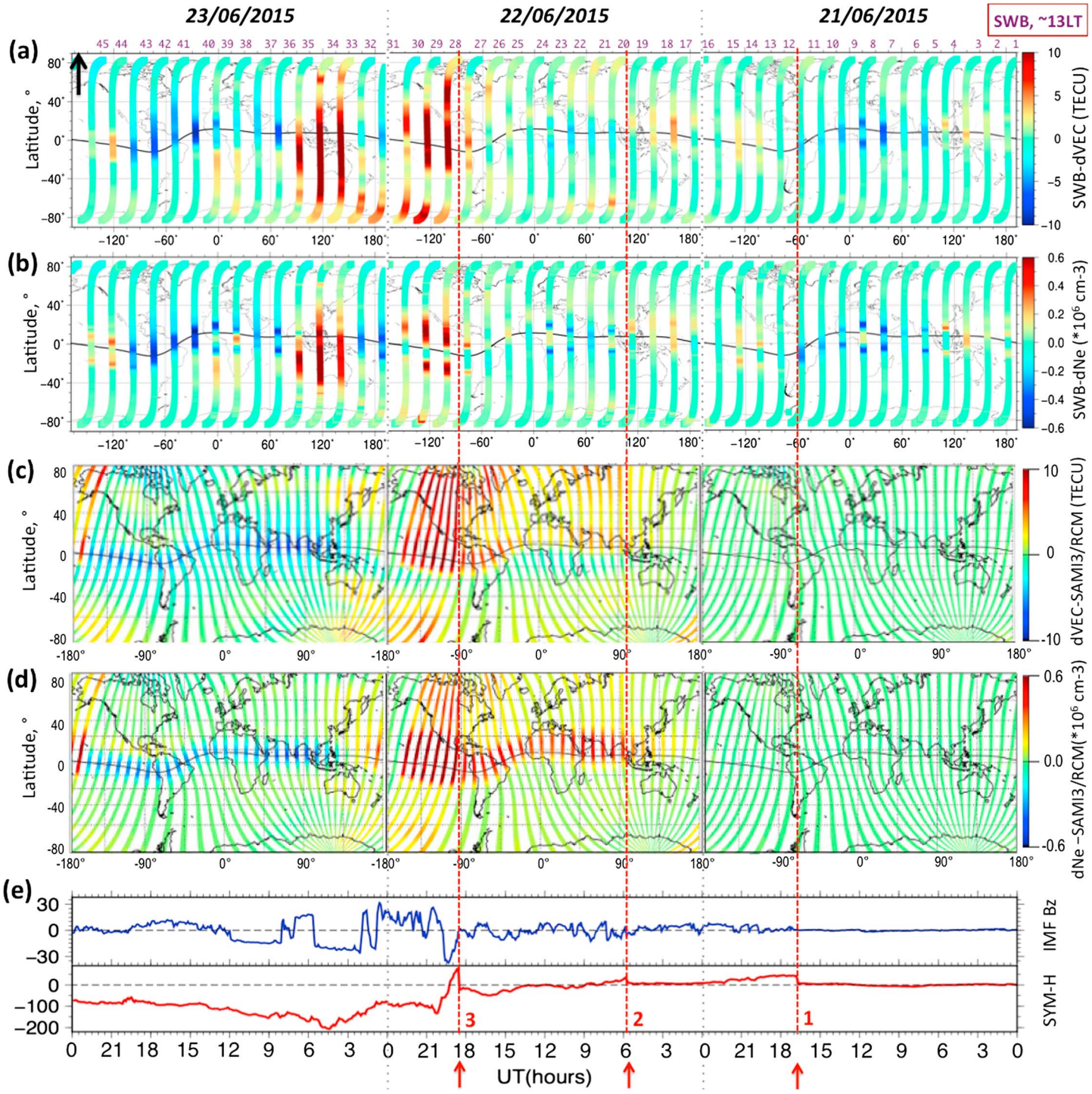

Figure 3. The same as Figure 2 but with the deviations (a, c) dVEC and (b, d) dNe parameters from the quiet time levels. Figures 3a and 3b show the SWB observations, and Figures 3c and 3d show SAMI3/RCM simulation results for the altitude of the SWB satellite.

positive ionospheric storm that lasted from ~18:30 to ~24:00 UT, the most pronounced effects were observed at low latitude and midlatitude and also at high latitudes in SH.

Tracks 31–32 (00:00–01:30 UT on 23 June) showed the occurrence of the negative ionospheric storm, as the equatorial and low-latitude VEC went below the quiet time values. Such result is not common for the dayside observations but in-line with ground-based observations. At the same time, at high latitudes in

SH the VEC continued to increase. From ~4 UT, and with the next IMF B_z southward turn, the second positive storm phase began (tracks 33–35 in Figures 2a and 3a). During this time, the SWB spacecraft flew over Asia and Australia and showed that VEC above 530 km increased up to 24 TECU (i.e., more than 100% increase as compared to the quiet time values, as seen in Figure S1). From ~7:30 UT, the SWB daytime measurements registered the beginning of the negative storm, which further lasted until the end of the day of 23 June 2015.

Figure 2b shows the "absolute" in situ Ne measurements from Swarm B for the 3 days under consideration, and Figure 3b shows the deviation electron density dNe as compared to the geomagnetically quiet day. The results in the Ne and dNe are similar to those in the VEC and dVEC, except for the high-latitude effects after the IS2, which are almost indiscernible (Figure 3b, tracks 20–24). The storm time effects in the Ne, both positive and negative, appear stronger than that in the VEC. Thus, with the beginning of the storm on 22 June, the Ne showed the occurrence and further reinforcement of the equatorial ionization anomaly (EIA), and the Ne within the EIA crests enhanced up to the maximum value of 1.2×10^6 cm^{-3}. From ~00:30 UT on 23 June strong negative disturbance at low latitudes occurred and lasted for 3–3.5 h (tracks 31–32). From ~4 UT, the equatorial and low-latitude electron density at the altitude of ~530 km increased again and lasted for the next 1.5 h. From ~7:30 UT we observed significant decrease of the low-latitude electron density, ~40% below the quiet time levels (Figure 3b, tracks 36–37). As in the VTEC measurements, the largest decrease in the Ne was observed at ~15–18 UT on 23 June.

Measurements of the ionospheric VEC and the electron density Ne by SWC in the ~11 LT sector and at/above ~460 km are shown in Figures 4a and 4b, respectively. The deviation values dVEC and dNe are shown in Figures 5a and 5b. Similarly to SWB results, the quiet time latitudinal profiles show hemispheric asymmetry with larger values in NH and a small quiet time increase at low latitudes in both VEC (up to 18 TECU) and Ne (up to ~$0.6–0.8 \times 10^6$ cm^{-3}). We observe the deviations from the background pattern following the arrival of the IS2, when the topside VEC increased at high latitudes in the NH. Unlike in the SWB results, with the arrival of the IS2, in SWC observations Ne increased over low latitude and midlatitude in the NH. This effect is particularly well seen in the dVEC results (Figure 5a, tracks 20–24): shortly after the arrival of the IS2, we observed ~5 TECU increase at high latitudes, and this enhancement seemed to propagate toward low latitudes during the next satellite passages. It is interesting to note that similar feature was observed in the GNSS-derived dVTEC (Animation S2). From ~6:30 to ~12:30 UT one can see a generation of ~10 TECU perturbation of over Europe and northern Africa.

From ~12 UT the topside VEC above SWC went back to the undisturbed level. Another small increase of the VEC at high latitudes in the NH was observed at ~14:30 UT (track 25); this enhancement was again registered during the following SWC daytime pass, in both VEC and Ne observations. We suggest that this enhancement was caused by the second strong enhancement of the *AE* index and the consequent auroral heating as described in section 3 and as seen in Figure 1i.

With the storm commencement, the first positive phase caused an increase of the topside VEC up to 30 TECU (Figure 4a), which is almost as twice as higher than the quiet time topside VEC (Figure 5a). Similarly to the SWB daytime measurements and also the ground-based GNSS-VTEC data, in the SWC results the first positive phase (tracks 28–29) was followed by the negative phase at low latitudes from 23 UT on 22 June to 1.5 UT on 23 June (tracks 30–32). From ~2:30 UT, we observe the second positive phase that lasted until ~5:30 UT (tracks 32–34). From ~6 UT the VEC and Ne decreased at all latitudes, and the strongest negative effects were observed at ~15–16 UT.

5.2. SAMI3/RCM Modeling of the Topside Ionosphere in the Daytime Sector

In Figures 2c and 2d we present modeling results for the time and longitude of Swarm B daytime passes shown in Figures 2a and 2b. The SAMI3/RCM estimated deviations dVEC and dNe are shown in Figures 3c and 3d.

The SAMI3/RCM results show quiet time variability of the VEC and Ne at ~530 km of altitude, with the maximum VEC value of ~15 TECU and maximum Ne of ~0.5×10^6 cm^{-3} reached around the magnetic equator. Figure 2c shows a small VTEC increase at high latitudes of NH following the arrival of the IS2. The low-latitude VTEC and Ne increased as well. The most striking feature is the storm time increases in VEC and Ne on 22 June 2015 in the equatorial Pacific sector at ~21:00 UT. This storm time effect is also quite pronounced in the dVEC

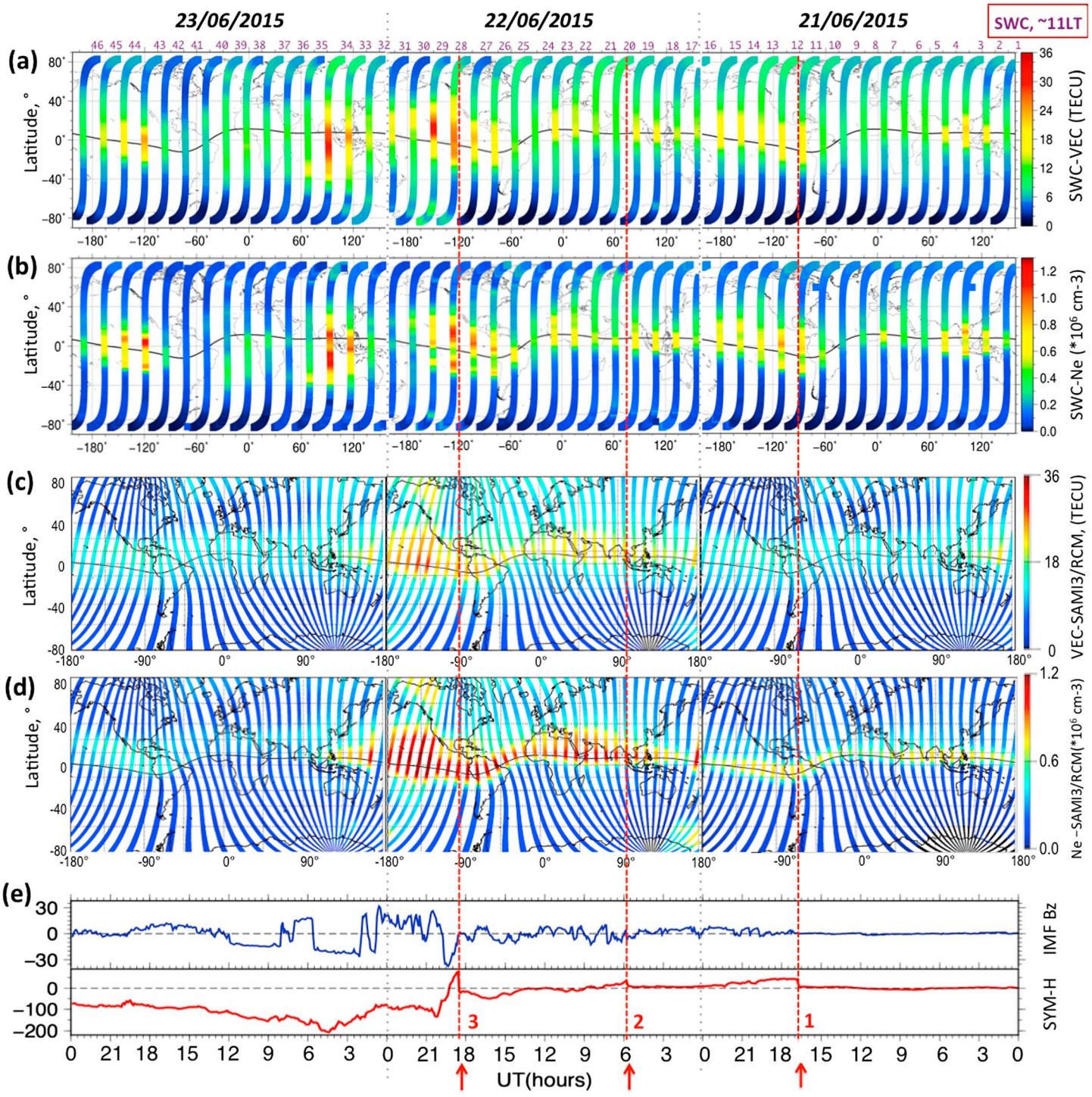

Figure 4. Ionospheric measurements by Swarm C (SWC) satellite during the daytime passes (equatorial crossing at ~11 LT) on 21–23 June 2015: (a) variations of the topside VEC above the SWC satellite altitude of ˜460 km as calculated from GPS receiver on board the satellite and (b) in situ electron density Ne as measured by the Langmuir probe on board SWC. Color shows the amplitude of the VEC (Figure 4a) and the Ne (Figure 4b), and the corresponding color scales are shown on the right side of the panels; SAMI3/RCM model-simulated VEC above (c) 460 km and the electron density Ne at the altitude of (d) 460 km. The presented tracks are the SAMI3/RCM simulations for the time and longitude at the equatorial crossings of the SWC satellite presented in Figures 4a and 4b; (e) variations of the IMF B_z component (blue curve) and *SYM-H* index (red curve). The dates are shown on the top of the figure, and the universal time (UT, running from right to left) is shown on the bottom. Red arrows and vertical red dashed lines indicate the time of arrivals of the three IS. The coordinates are geographic.

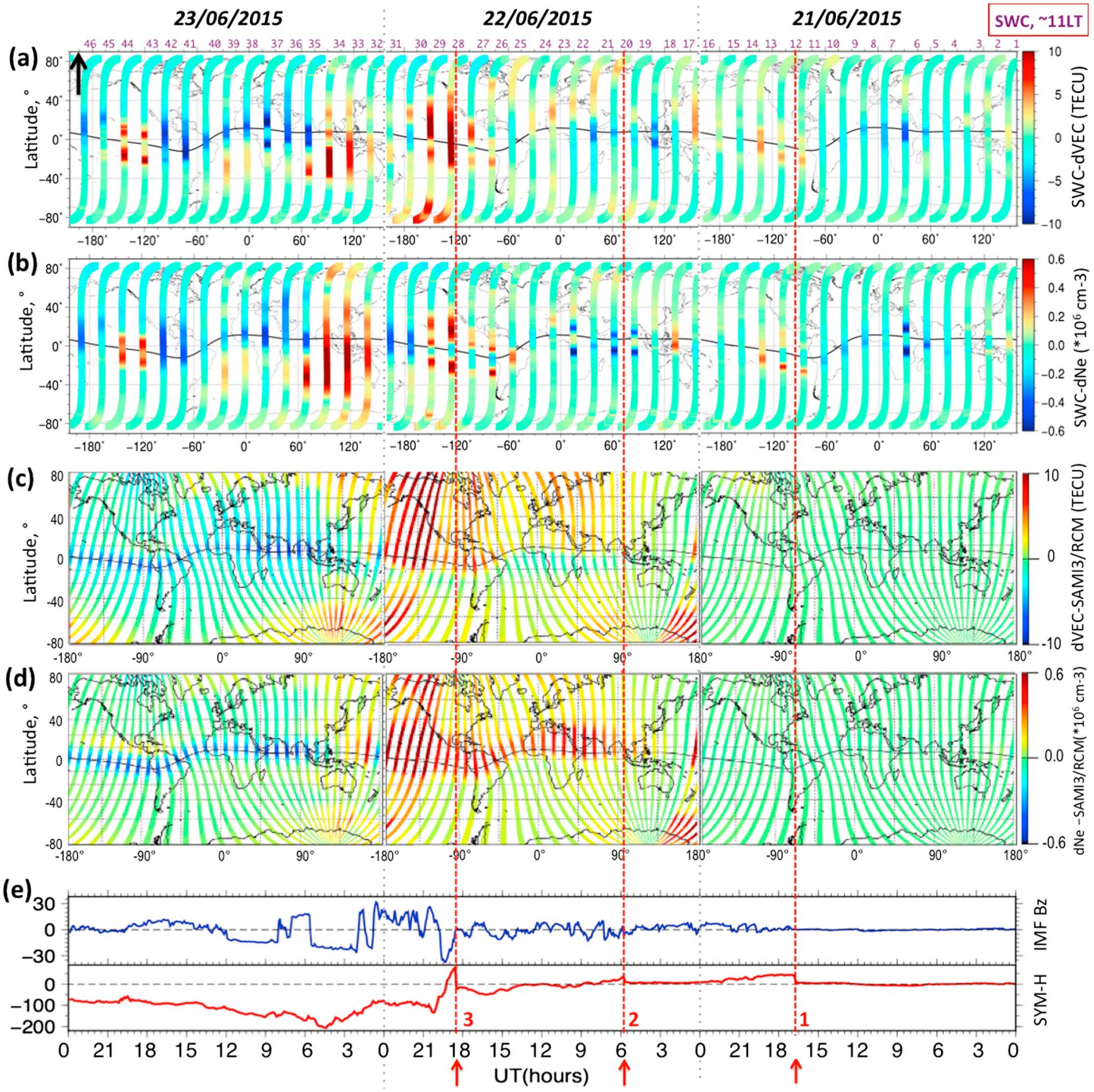

Figure 5. The same as Figure 4 but for the deviations (a, c) dVEC and (b, d) dNe parameters from the quiet time levels. Figures 5a and 5b show the SWC observations, and Figures 5c and 5d show the SAMI3/RCM simulation results at the altitude of SWC.

and dNe results (Figures 3c and 3d). This increase occurs at the beginning of the storm between 18:40 UT and 24:00 UT on 22 June 2015 and is caused by a storm time penetration electric field (Huba et al., 2016; Huba & Sazykin, 2014). Similarly to the Ne Swarm B observations, the SAMI3/RCM model results show the occurrence of the two crests of the EIA and a strong overall enhancement of the low-latitude VEC (Figures 2b and 2d). This enhancement continues until the beginning of the next day, when both VEC and Ne go back down to the quiet time values, which also agrees with observations. Meanwhile, the storm time effects at high

latitude and midlatitude of NH seem to be overestimated in the SAMI3/RCM results. Also, the second positive storm that was observed over Asia from ~3 to ~7 UT on 23 June 2015 is not reproduced by the SAMI3/RCM. Instead, a long-term negative storm can be seen throughout 23 June at low latitudes. The model, however, reproduces the enhancement in low-latitude VEC and Ne at the end of 23 June at 21–23 UT, which is consistent with the observations.

In Figures 4c and 4d we present modeling results computed for the altitude of the Swarm C and for the time of the dayside passes, and Figures 5c and 5d show the SAMI3/RCM estimated deviations dVEC and dNe. The qualitative results for the SWC altitude are similar to those calculated for the SWB altitude and local time. However, because Swarm C is at a lower altitude than Swarm B, the VEC is slightly larger in SWC results and the magnitude and the extent of the electron density is larger. The disturbance time effect is especially strong in the storm-to-quiet values (Figures 5c and 5d).

5.3. Ionospheric Swarm Observations in the Nighttime Sector

Figure 6a shows variations of the topside VEC above the Swarm B satellite during nighttime passes (above ~530 km of altitude, in the ~01 LT sector) for the period of time from 21 to 23 June 2015. The corresponding dVEC results are shown in Figure 7a. The quiet time VTEC values for the day of 20 June 2015 can be found in Figure S1 (supporting information). One can see that the first deviation of the VEC from the quiet time pattern occurred at high latitudes at ~8.5 UT on 22 June in both NH and SH (track 21, Figures 6a and 7a). This high-latitude increase was followed by the low-latitude VEC enhancement up to ~10–11 TECU that lasted from ~9.5 UT to ~11:30 UT (tracks 22–23, Figures 6a and 7a). We consider this VEC enhancement to be caused by the IS2 arrival and the consequent increase of the auroral and substorm activity, as discussed below.

In these nighttime SWB observations, another small VEC increase that exceeds the background level can be seen at ~16–18 UT on 22 June (tracks 26–27). This should be caused by the second enhancement of the auroral activity that lasted from ~14 UT to 17 UT (Figure 1i). These results are similar to the daytime observations on SWB.

With the beginning of the storm at ~18:38 UT, the nighttime SWB measurements first show positive storm effects at high latitudes of the SH and midlatitudes in NH and small negative effect at low latitudes (tracks 29–30, Figure 6a). From ~23.2 UT the VEC at high latitude and midlatitude of the NH started to increase, and it reached ~16–18 TECU at low latitudes by ~1–3 UT on 23 June (Figure 6a, tracks 31–34), which is ~200–300% increase as compared to the quiet time values (Figure 7a, tracks 31–34). It should be noted that this enhancement over south European and North African regions are in agreement with the data of ground-based GNSS receivers. The observed nighttime topside VEC behavior corresponds to polarity changes of the IMF B_z and the IEF E_y components. One can see that the first nighttime ionospheric suppression occurred during the IEF E_y positive value, indicating the effect of the prompt penetration of the interplanetary electric fields, which is positive on the dayside and negative on the nightside (e.g., Kikuchi & Hashimoto, 2016). The consequent change of the IEF polarity caused suppression on the dayside and an uplift on the nightside.

From ~4 UT, the VEC started to gradually decrease, and from 5.5 UT the VEC reached the quiet time values and even went slightly below them later on 23 June (Figure 7a). Another small low-latitude VEC increase was observed at 11–12 UT over Pacific region.

The Ne measurements are shown in Figure 6b, and the Ne deviations (dNe) are presented in Figure 7b. The general Ne behavior during the days of observations is similar to that of the VEC: we observe a strong response at low latitudes of the NH ~2–3 h after the IS2 arrival and a smaller second effect at 16–17 UT on 22 June due to the second *AE* enhancement. The storm time first negative storm is stronger in Ne than in VEC, and this effect is especially obvious from the dNe results (Figure 7b). The Ne enhancement over Africa and Atlantic region from ~0.5 UT to ~4.5 UT on 23 June is quite pronounced. Similarly to the VEC observations, we observe a Ne enhancement around 12 UT on 23 June, and small negative effect is visible until the end of the day.

Swarm C measurements are shown in Figures 8a and 8b, and dVEC and dNe data are shown in Figures 9a and 9b. The quiet time VEC values for the day of 20 June 2015 can be found in Figure S2 (supporting information). The quiet time nightside VEC latitudinal profile from SWC shows an asymmetric behavior with higher VEC values in the NH, and the maximum of ~10–13 TECU at low latitudes (Figure 8a). The arrival of

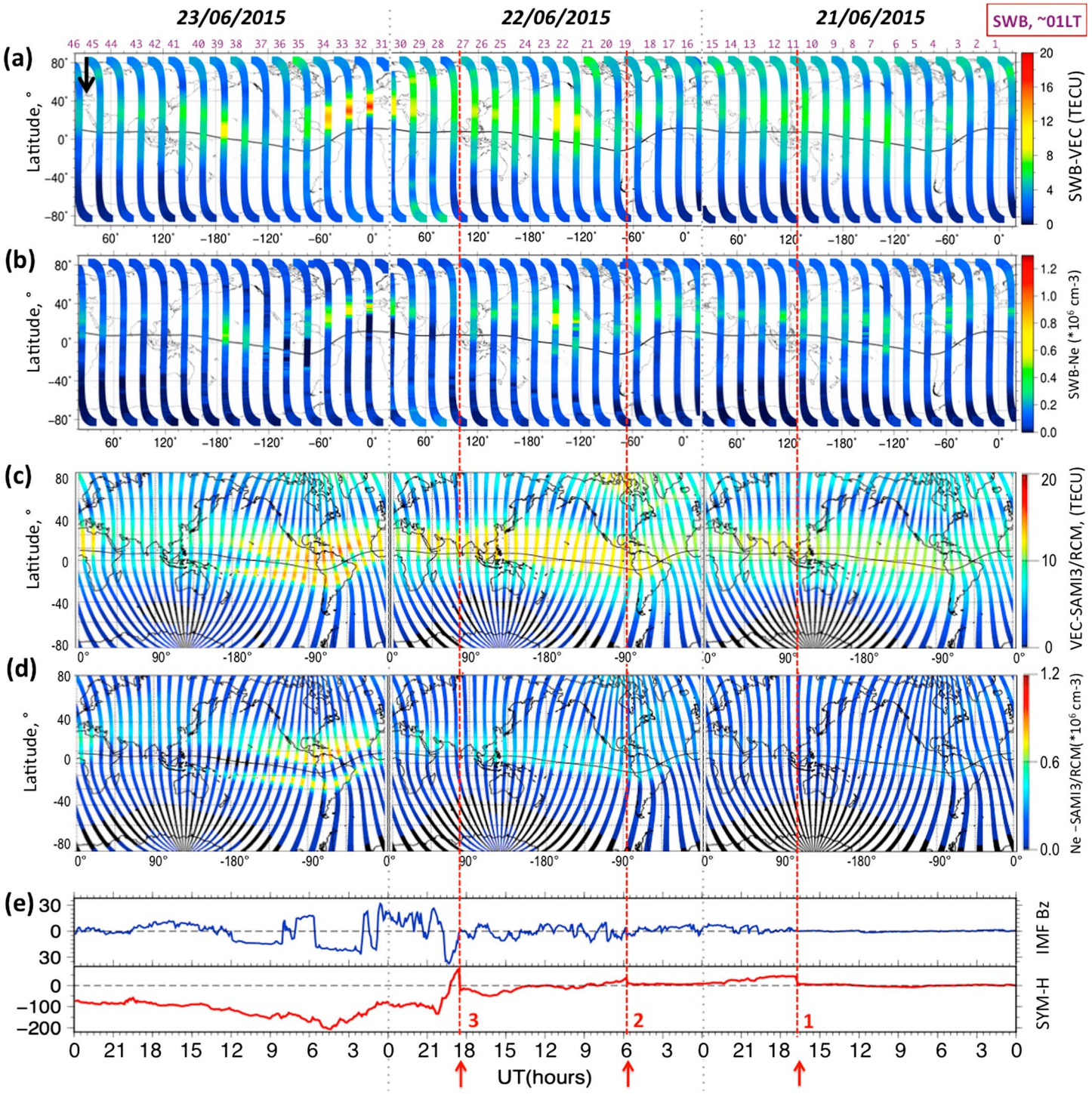

Figure 6. Ionospheric measurements by Swarm B (SWB) satellite during the nighttime passes (equatorial crossing at ~01 LT) on 21–23 June 2015: (a) variations of the ionospheric VEC above the Swarm B satellite altitude of ~530 km as calculated from GPS receiver on board the satellite and (b) in situ electron density Ne as measured by the Langmuir probe on board SWB. Color shows the amplitude of the VEC (Figure 6a) and the Ne (Figure 6b), and the corresponding color scales are shown on the right side of the panels. Violet numbers on the top show satellite track number. Black arrow in the top left panel shows the direction of the satellite movement, ascending or descending; SAMI3/RCM model-simulated VEC above (c) 530 km and the electron density Ne at the altitude of (d) 530 km for the time period 21–23 June 2015. The presented tracks are the SAMI3/RCM simulations for the time and longitude at the equatorial crossings of the SWB satellite presented in Figures 6a and 6b; (e) variations of the IMF B_z component (blue curve) and *SYM-H* index (red curve) on 21–23 June 2015. The dates are shown on the top of the figure, and the universal time (UT, running from right to left) is shown on the bottom. Red arrows and vertical red dashed lines indicate the time of arrivals of the three IS. The coordinates are geographic.

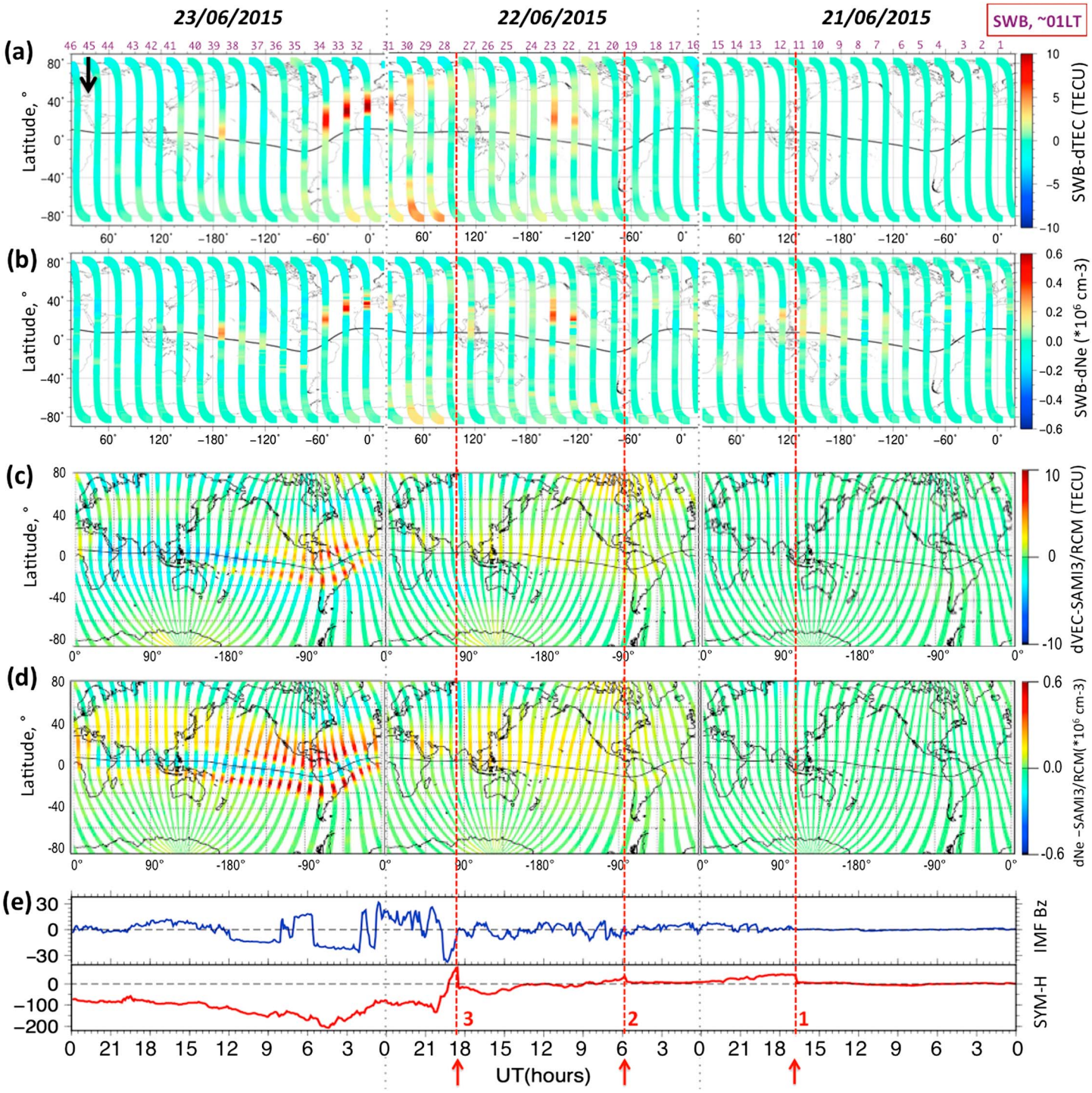

Figure 7. The same as Figure 4 but for the deviations (a, c) dVEC and (b, d) dNe parameters from the quiet time levels. Figures 7a and 7b show the SWB nighttime observations, and Figures 7c and 7d show the SAMI3/RCM simulation results.

the second IS at 5:45 UT on 22 June provoked the first alteration from the quiet time pattern. First, VTEC increased at high latitudes in both NH and SH (observed at ~7.3 UT, track 21). Second, by 9 UT, the low-latitude and midlatitude VEC increased up to 19 TECU (track 22, Figure 8a). During the next nighttime pass of SWC, the low- to middle-latitude VEC decreased to 14–15 TECU (track 22, Figure 8a). The second *AE* enhancement is seen in the SWC VEC data as a small VEC increase over midlatitudes in NH (track 27).

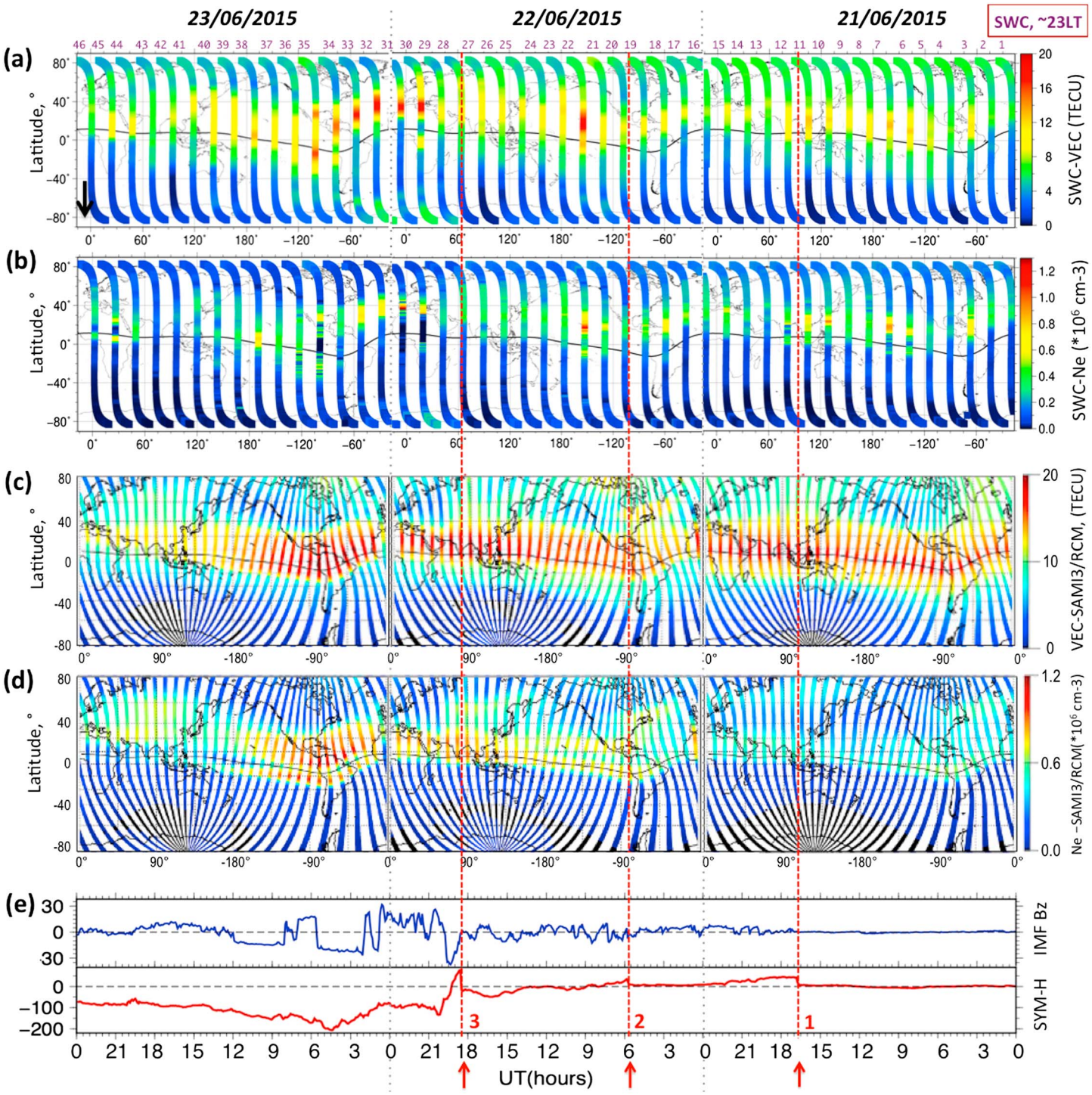

Figure 8. Ionospheric measurements by Swarm C (SWC) satellite during the nighttime passes (equatorial crossing at ~23 LT) on 21–23 June 2015: (a) variations of the topside VEC above the SWC satellite altitude of ~460 km as calculated from GPS receiver on board the satellite; (b) in situ electron density Ne as measured by the Langmuir probe on board SWC. Color shows the amplitude of the VEC (Figure 8a), the Ne (Figure 8b), and the corresponding color scales are shown on the right side of the panels; SAMI3/RCM model-simulated VEC above (c) 460 km and the electron density Ne at the altitude of (d) 460 km. The presented tracks are the SAMI3/RCM simulations for the time and longitude at the equatorial crossings of the SWC satellite presented in Figures 8a and 8b; (e) variations of the IMF B_z component (blue curve) and *SYM-H* index (red curve). The dates are shown on the top of the figure, and the universal time (UT, running from right to left) is shown on the bottom. Red arrows and vertical red dashed lines and labels 1, 2, and 3 indicate the time of arrivals of the three IS. The coordinates are geographic.

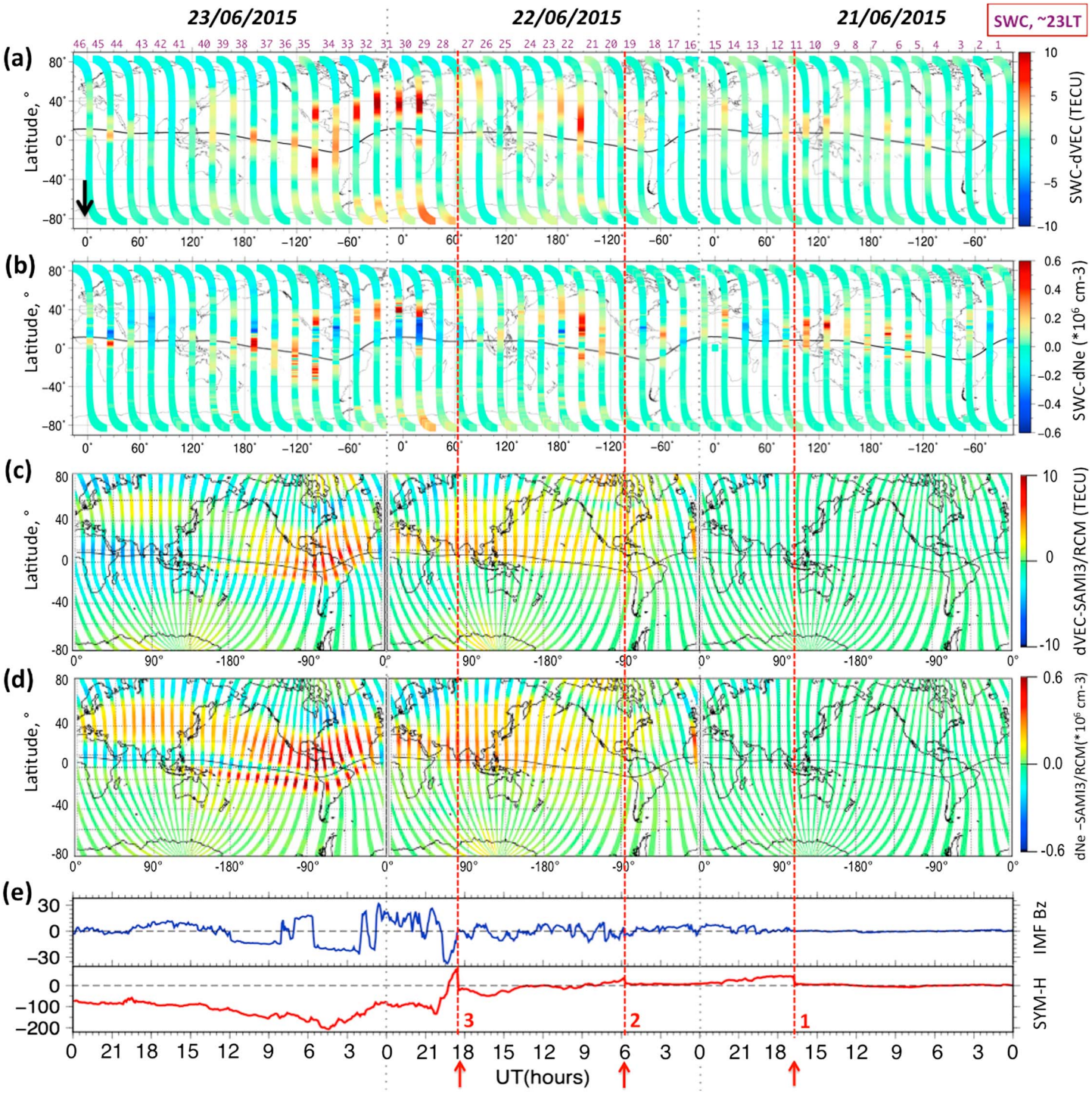

Figure 9. The same as Figure 4 but for the deviations (a, c) dVEC and (b, d) dNe parameters from the quiet time levels. Figures 9a and 9b show nighttime SWC observations, and Figures 9c and 9d show the SAMI3/RCM simulation results.

Within the first 1–1.5 h after the development of the storm, no clear effect occurred in the VTEC (track 29, Figures 8a and 9a). However, from 21:20 UT a strong enhancement of the low-latitude VEC, with a development of the two-peak EIA can be seen in the SWC data (track 29). From ~23 UT, only effects in the NH can be seen, where the VEC reached ~18–19 TECU (i.e., more than 100–150% increase as compared to the quiet time level). The storm time low-latitude VEC enhancement continued until ~12 UT of 23 June. From ~14 UT on 23

June and with the development of the recovery phase, the VEC decreased to prestorm values and even lower (Figures 8a and 9a).

The in situ electron density measurements from SWC and their deviations from the quiet time values are shown in Figures 8b and 9b, respectively. The first strong increase up to 1.2×10^6 cm^{-3} occurred at ~9 UT on 22 June, which is, most likely, related to the ionospheric response to the substorm that was generated by the IS2. The dNe results clearly show the development of the EIA during this moment of time (track 22, Figure 9b). The Ne remained enhanced for several hours more in the NH, and it then decreased to the quiet time values. From ~21 to 22 UT on June 22, complex effects occurred in the electron density: the Ne significantly decreased over magnetic equator and it increased within the crests of the EIA. These observations are the indications of the development of the EIA and of the ionospheric uplift at equatorial and low latitudes. Similar effect occurred at ~5.2–6 UT on 23 June (track 35). These nighttime observations are interesting and rather rare. Comparison of day and nightside observations reveals that during this period of time, from ~4 to ~6 UT we observed a strong ionospheric increase and the uplift on the dayside, which we attributed to the PPEF. This same PPEF effect should have normally caused a downward plasma drift on the nightside with consequent suppression of the EIA and further development of the negative ionospheric storm. However, Figures 8a, 8b, 9a, and 9b, tracks 34–35, show signatures of ionospheric uplift over the equator (track 34, time of the pass is 3.6 to 4.38 UT) and the EIA development (track 35, from 5.16 to 5.95 UT). Based on these observations, we consider that this nighttime increase could be assisted by the action of the disturbance dynamo effect that was already developed at this stage of the storm. It is known that the disturbance dynamo effect develops over a period of hours after the beginning of a storm, and it generates westward equatorial electric fields on the dayside and eastward electric fields on the nightside (e.g., Blanc & Richmond, 1980; Maruyama et al., 2005). Once developed, the disturbance dynamo electric fields would compete with the PPEF or reinforce the PPEF effect, depending on the IMF polarity and day/night conditions. Otherwise, the time delay between the PPEF action and the ionospheric response should also be taken into account while explaining the topside results.

The storm time effects continued until ~12 UT on 23 June, and from that time, the Ne decreased to prestorm values. Figures 9a and 9b demonstrate rather strong negative effects at low latitude and midlatitude from ~7 to 17 UT on 23 June.

5.4. SAMI3/RCM Modeling of the Topside Ionosphere in the Nighttime Sector

In Figures 6c and 6d we present modeling results for the time, altitude, and longitude of Swarm B nighttime passes. The SAMI3/RCM estimated deviations dVEC and dNe are shown in Figures 7c and 7d.

Compared to the daytime results shown in section 5.2 both the VEC and electron density are reduced, as expected. Figures 7c and 7d show no effect caused by the IS1, which is consistent with the observations (Figures 7a and 7b). Then, following the arrival of the IS2, the VEC increased at low latitudes and at high latitudes in NH. Compared to the SWB observations, this effect seems to be somewhat overestimated in the modeling results, as the VEC remained increased until the beginning of the geomagnetic storm at 18:38 UT on 22 June. This small long-term increase is also seen in the dVEC and dNe parameters (Figures 7c and 7d).

With the storm commencement, the absolute VEC first decreased as compared to the prestorm values, which is similar to the observational results. The negative perturbation at midlatitudes is clearly seen in the dVEC and dNe parameters (Figures 7c and 7d), while the dVEC and dNe around the magnetic equator remained ~2 TECU enhanced as compared to the quiet time values. From ~0 UT to ~10 UT on 23 June, the SAMI3/RCM results show in both absolute and deviation results an enhancement at low latitudes and decrease over the magnetic equator. These results are probably due to the model calculating larger equatorial upward drift than expected which causes enhanced densities at higher altitudes. Note that this modeled effect is asymmetric as it extends to midlatitudes in the NH. These SAMI3/RCM simulations differ from the SWB results. First, the nightside modeling results have values of VEC and Ne a bit larger than those measured on Swarm B (Figures 7a and 7b). Second, the observations show low-latitude and midlatitude increase only in NH and only from 0 to 5 UT.

In Figures 8c and 8d we present modeling results for the time and longitude of Swarm C nighttime passes shown in Figures 8a and 8b. The corresponding deviation parameters dVEC and dNe estimated from

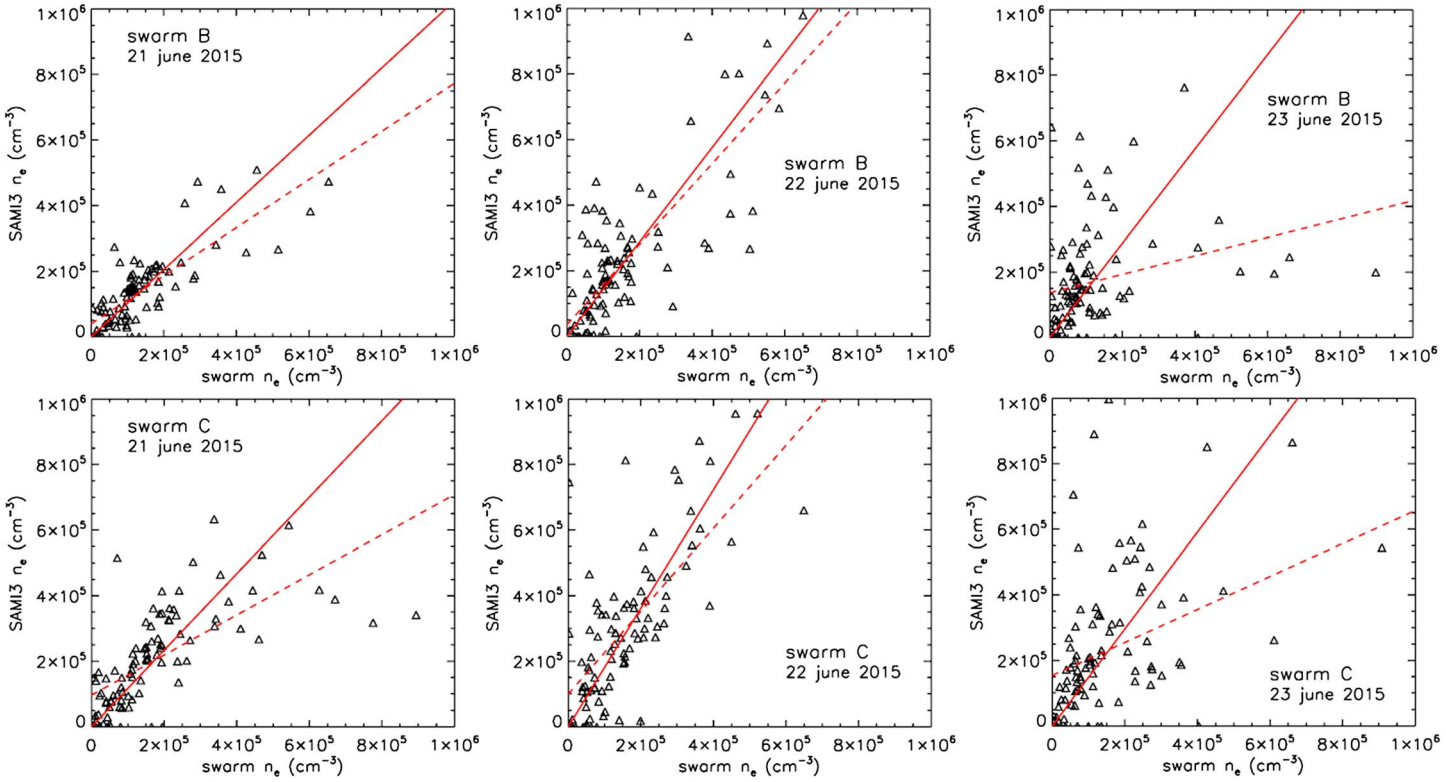

Figure 10. Scatterplots of Swarm B and C data versus SAMI3 simulation results at roughly the same location and time. (top row) For Swarm B at ~530 km and (bottom row) for Swarm C at ~460 km. The solid red line is based on the equation $y = Mx$, where $M = Sy/Sx$ and Sy = mean (SAMI3/RCM Ne) and Sx = mean (Swarm Ne). The dashed red line is the linear least squares fit to the data.

SAMI3/RCM model can be found in Figures 9c and 9d. One can see that the SWC nighttime simulations are similar to SWB nighttime results, but the VEC and Ne are larger here because Swarm C is at a lower altitude. In this LT sector and at this altitude, we can see rather big discrepancies between the observations and the SAMI3/RCM modeling results. The modeled VEC at low latitudes is largely overestimated during both quiet and storm conditions. The electron density agrees better with the observations. The difference can also be seen in the ionospheric behavior to the IS2 arrival; as in SAMI3/RCM simulations this effect is less obvious than in the observations (Figures 8c, 8d, 9c, and 9d).

The storm time SAMI3/RCM simulated effect at SWC altitude is quite similar to that at SWB altitude: we first observe negative effects in VEC at midlatitude and especially in the Ne this negative perturbation is strong (Figure 9d). From ~2 UT, one can observe significant enhancements in the VEC and Ne. The EIA is clearly evident in the electron density at ~1–10 UT in the American sector on 23 June 2015. Comparison to the quiet time values shows quite significant storm time effect in the EIA region during this moment of time (Figure 9d). Again, these modeling results have values of VEC and Ne quite a bit larger than those measured on SWC.

5.5. Comparison of Swarm and SAMI3/RCM Results for the Electron Density

In Figure 10 we present scatterplots of SWB and SWC data versus SAMI3/RCM simulation results at roughly the same location and time, for the time period from 21 to 23 June 2015. SAMI3/RCM output cadence is 15 min so there is a limited amount of simulation data compared to the Swarm satellite data set. Figure 10 (top row) are for Swarm B at ~530 km and Figure 10 (bottom row) are for Swarm C at ~460 km. The solid red line is based on the equation $y = Mx$, where $M = Sy/Sx$ and Sy = mean (SAMI3 Ne) and Sx = mean (Swarm Ne). The dashed red line is the linear least squares fit to the data.

On 21 June 2015 the comparison between the data and model results is reasonably good, especially for Ne $\leq 4 \times 10^5$ cm^{-3}. On this day $M \sim 1$; the slope of the least squares fit curve is <1 primarily because of

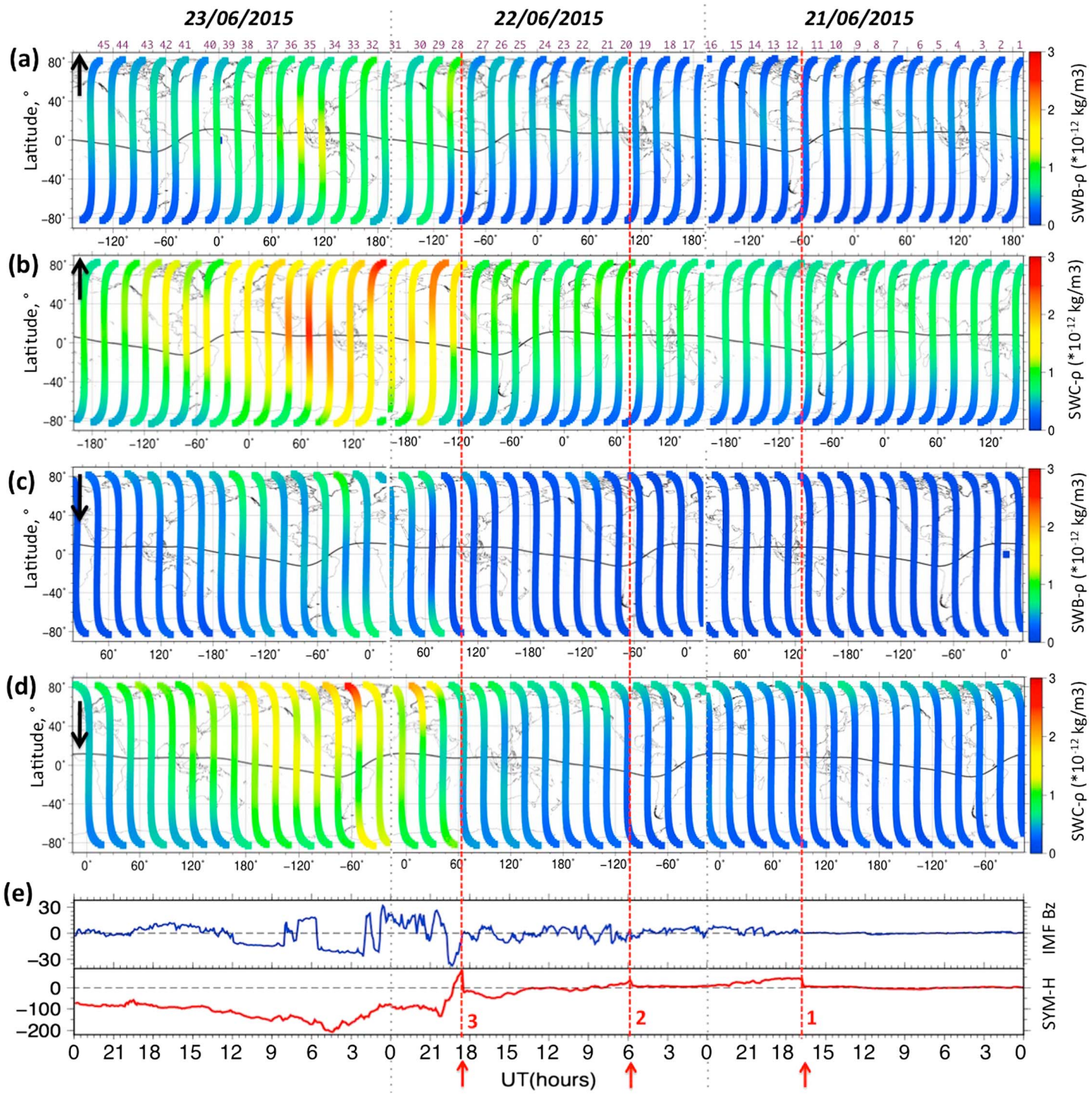

Figure 11. (a–d) Variations of the thermospheric neutral mass density (ρ) as derived from the GPS receivers on board Swarm spacecraft during 21–23 June 2015: (a, b) dayside measurements from SWB (at ~530 km, equatorial crossing at ~13 LT) and SWC (at ~460 km, equatorial crossing at ~11 LT) and (c, d) nightside measurements from SWB (~01 LT) and SWC (~23 LT), respectively. Black arrows on the left show the satellite movement direction, ascending and descending. The color scale is shown on the right; (e) variations of the IMF B_z component (blue curve) and *SYM-H* index (red curve). The UT scale is shown on the bottom of the figure; time is running from right to left. Red vertical dashed lines show the arrival time of the three IS, as noted by "1," "2," and "3." Gray vertical dotted lines show the 24 UT timelines, and the dates are shown on the top of the figure. Violet numbers on the top show satellite track numbers.

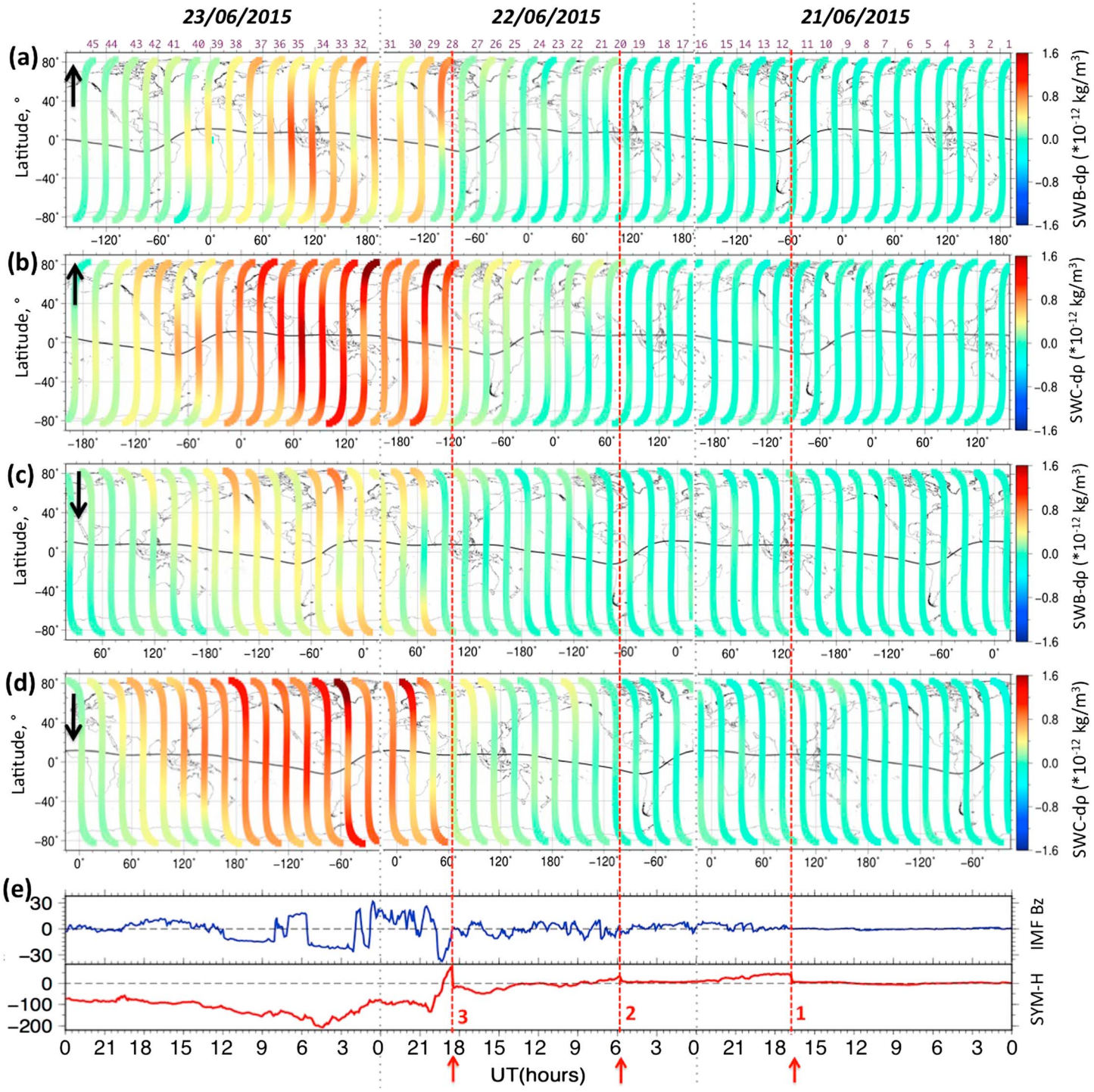

Figure 12. The same as Figure 11 but for the deviations dρ of the neutral mass density from quiet time values.

higher Swarm densities (i.e., $>6 \times 10^5$ cm^{-3}). On the large storm day 22 June 2015 there is a significant increase in the SAMI3/RCM density relative to the Swarm densities. The slope M is ~1.3 for SWB and ~1.7 for SWC; additionally, the slope of the least squares fit line is close to M. The increase in the SAMI/RCM electron density is attributed to the penetration electric field, which acts to "lift" electrons in the low- to middle-latitude ionosphere. On 23 June 2015 there is a much larger spread in the densities for Ne $> 3 \times 10^5$ cm^{-3}. This may be due to the disturbance dynamo associated with storm time modification

of the thermospheric winds that are not accurately captured in the SAMI3/RCM model. Lastly, we again note that the SAMI3/RCM simulation study used an aligned, untilted dipole model for the geomagnetic field. The results were mapped to the IGRF using the Richmond apex model in order to compare with the Swarm data, and this mapping could also account for some of the disparity between the observational data and model results.

6. Thermospheric Response to the 21–23 June Geomagnetic Disturbances

Figures 11 and 12 show variations of the thermospheric neutral mass density ρ and their deviations from the quiet time values $d\rho$, respectively. Figures 12a and 12b show daytime passes of SWB and SWC, and the nighttime passes for SWB and SWC are shown in Figures 12c and 12d. The quiet time values observed on 20 June 2015 can be found in Figures S1c, S1f, S2c, and S2f.

One can see that with the arrival of the IS2 the neutral density slightly increased in the NH in all observations, except for the SWB nightside results (Figures 11 and 12). The substorm effects appeared stronger in the SWC data (Figures 12b and 12d). We suggest that these enhancements of the neutral mass density are due to enhanced auroral activity during this periods of time, as can be seen in Figure 1. It should be noted that these nighttime ρ enhancements coincide with the high-latitude VEC and Ne increases (Figures 6–9).

The most significant thermospheric effects occurred after the geomagnetic storm onset at 18:38 UT on 22 June, when the neutral density largely increased at high latitudes in both hemispheres. Then, within several hours, the "bulge" spread to middle and low latitudes. The storm time effects were stronger in data of the lower satellite SWC, where the neutral mass density increased for ~300–500% throughout all latitudes on both dayside and nightside (Figures 12b and 12d).

It is interesting to note that in the dayside SWB and SWC observations the strongest ρ increases up to ~1.4×10^{-12} kg/m3 (SWB) and up to 3×10^{-12} kg/m3 (SWC) occurred by 4.5–7 UT at equatorial and low latitudes, when the satellites flew over Asian region (tracks 34, 35, Figures 11a and 11c). It should be pointed out that we observed VEC and Ne enhancements over this region and during this period of time (Figures 2–5).

The dayside storm time enhancement in the neutral mass density lasted until ~12 UT and then started to gradually diminish, although the thermospheric density remained increased until the end of day of 23 June.

7. Discussions and Conclusions

On 21–23 June 2015, three IS arrived at Earth. The first IS was recorded at 16:45 UT on 21 June 2015 and only caused ~50 nT increase in the *SYM-H* index. The second IS arrived at 5:45 UT on 22 June and generated an enhancement of the auroral and substorm activity. The third and much larger IS arrived at 18:38 UT on 22 June. Followed by a giant CME, it was accompanied by large-amplitude fluctuations of the IMF B_z component and initiated a major geomagnetic storm that lasted for many hours.

Here by using a set of ground-based and spaceborne instruments, we studied ionospheric and thermospheric behavior during the period of time from 21 to 23 June 2015. We compare our observations with simulation results by the SAMI3/RCM model.

We observed several interesting features during the considered period of time:

1. The arrival of the IS2 and the consequent substorm development led to small increases in the thermospheric neutral mass density at high latitudes and more pronounced effect in the ionospheric parameters VTEC and electron density. The substorm ionospheric effect first occurred at high latitudes, and several hours later, it spread to middle and low latitudes. It is interesting to note that on the dayside only SWC results showed the IS2 effect, and not SWB. On the nightside, the IS2 effect was observed in data of both satellites, and it was particularly strong in SWC data, where it was comparable with the storm time alterations. The observed stronger nightside effect is, most likely, related to the fact that during a substorm, the energy is deposited in the auroral region on the nightside near the midnight sector, which leads to response being focalized around the midnight meridian. However, substorms can cause effects on the dayside as well.

It is known that during substorms the energy input from the solar wind into the upper atmosphere is most efficiently coupled into the high-latitude ionosphere-thermosphere system. Associated with the substorms

locally enhanced electric fields, particle precipitation, and field-aligned and electrojet currents lead to the thermosphere expansion, to generation of traveling atmospheric disturbances (TADs) and to enhancement of the meridional thermospheric winds. These changes occurring primarily at high latitudes are further transferred by the enhanced meridional neutral winds and TADs toward midlatitude and even low latitude. The thermospheric substorm alterations consequently impact the ionospheric behavior at high and middle latitudes and also at equatorial and low latitudes through the disturbance dynamo effect (Sastri et al., 2003; Sobral et al., 1997). Substorms are also known to cause the penetration of magnetospheric electric fields to low-latitude ionosphere, which consequently affects the ionospheric plasma distribution at the equatorial and low latitudes (e.g., Kikuchi & Hashimoto, 2016).

Our thermospheric observations are in agreement with previous results from CHAMP satellite measurements (Clausen et al., 2014; Ritter et al., 2010) and also with modeling results (e.g., Fuller-Rowell & Rees, 1981). Thus, Ritter et al. (2010) showed that following a substorm, the thermospheric neutral mass density is first enhanced at high latitudes. They also found that the thermospheric response is maximal around the midnight local magnetic time; however, it is less developed in the premidnight sector (~22.5 magnetic local time (MLT)) and much less visible in the postmidnight sector (~01 MLT). The latter observation demonstrates that even at the same altitude, there can be a substantial difference in the local time response, even if the LT regions are only separated by 1–2 h. This result might also explain the difference in our observations between SWC and SWB satellites. Ritter et al. (2010) also showed that from the high latitude the thermospheric disturbance/bulge traveled at an average speed of 650 m/s to lower latitudes and 3–4 h later the bulge reached the equator on the nightside. However, in the data of SWB and SWC we only observed a descent of the neutral mass density bulge to midlatitudes, while low latitudes did not seem to be concerned by the thermospheric changes. Instead, the nightside ionospheric parameters increased at low latitudes ~2–3 h following the substorm onset, which makes us conclude on the thermosphere driving this low-latitude enhancement in the topside ionosphere. Interestingly, on the dayside, we observe the generation of the bulge and its further descent to lower latitudes in the ionospheric measurements.

It should be noted that the ionospheric response to substorm can vary depending on altitude. Schunk et al. (1997) simulated ionospheric response to a substorm in the auroral region and found that during the substorm expansion phase the *E* region densities increased due to auroral particle precipitation, while the plasma densities above 300 km decreased due to the overall lowering of the ionosphere. In our case, we first observed small increase in the topside ionosphere at high latitudes, which was followed by much stronger enhancement in the topside low-latitude ionosphere. It is difficult to confirm this topside effect observed over the Pacific region by ground-based measurements because of the lack of GNSS receivers in that region. At least, the GNSS-derived VTEC data above the Hawaiian Islands do not seem to show the IS2-related changes (Animations S1 and S2). Interestingly, the SAMI3/RCM model showed small enhancements in the topside VEC and Ne; however, in the total VTEC the effects are much less visible, which is quite similar to the observations.

2. During the 22–23 June geomagnetic storm, data from ground-based GNSS receivers and dayside satellite observations show that at low and middle latitudes, the storm consisted of two consequent positive and negative phases. The occurrence of the first positive and negative phases is in agreement with variations of the IMF B_z and the IEF E_y, which indicates the large impact of the prompt penetration electric fields on the ionosphere and the topside ionosphere at the beginning of this storm.

The second strong low-latitude ionospheric enhancement was observed in Asian-Australian region from ~2:30 to ~7:30 UT on 23 June, that is, at the end of the main phase and at the beginning of the recovery phase of the storm. Global VTEC maps clearly show that this effect was hemispherically asymmetric, as a very significant positive storm was observed in winter hemisphere, while in summer hemisphere the storm time dVTEC increase was quite moderate (Animation S2). The occurrence of this huge low-latitude positive effect and its disappearance correspond to the time of the second long-term IMF B_z negative event that was observed from ~1:50 to ~5:45 UT (Animation S2). The low-latitude VTEC started to increase ~30–40 min after the IMF B_z turned southward, and the positive effect started to diminish almost immediately after the northward turn of the IMF B_z, and fully disappeared by 7:45 UT (Animation S2). Therefore, we conclude that this second positive ionospheric storm was largely driven by the PPEF effect enhancing the equatorial zonal electric fields. It is known that on the dayside, the enhanced eastward electric field increases the upward E × B

drift that uplifts the low-latitude plasma to higher altitudes, where the recombination in slower, while the solar radiation continues to ionize the lower altitude plasma leading to the overall increase of the VTEC. However, the PPEF action should also cause the superfountain effect (Tsurutani et al., 2004), which does not seem to be case. In addition, we observed the hemispheric asymmetry in the response. These facts lead us to conclusion that the observed effect was, most likely, driven by a combination of the PPEF and summer-to-winter thermospheric winds. The latter can be particularly enhanced during storm time at solstice conditions. The equatorward neutral winds push ions and electrons up along magnetic field lines from high to middle and low latitudes and cause positive storms. Comparison of Figures 2–9, 11, and 12 reveals that the ionospheric enhancement observed over the Asian region corresponds in time and in spatial location to the increase of the thermospheric neutral mass density. These facts might indicate on a large influence of the thermospheric drivers on the observed topside VEC and Ne enhancements at this stage of the storm.

In addition to neutral winds, the thermospheric composition is known to play a role in driving the positive ionospheric storms. The prevailing summer-to-winter thermospheric winds transport the molecular rich gas to middle and low latitudes in the summer hemisphere following the day or two following the storm (Fuller-Rowell et al., 1996). In the winter hemisphere, poleward winds restrict the equatorward movement of composition. The altered neutral-chemical environment in summer subsequently depletes the *F* region midlatitude ionosphere and leads to the occurrence of a negative phase. In winter midlatitudes a decrease in molecular species, associated with downwelling, persists and produces a positive phase. In the case of June 2015 storm, the Global Ultraviolet Instrument showed that on 23 June the thermospheric O/N_2 ratio significantly increased in the winter hemisphere, especially over Australia and over the Indian Ocean, which, indeed, proves the large impact of thermospheric winds during the June 2015 storm (Astafyeva et al., 2016).

It is interesting to note that during the occurrence of this strong positive ionospheric storm in the Asian region, we observe a strong negative storm over northern Europe that lasted from ~3 to 8 UT (Animation S2). This VTEC decrease occurred in the early morning sector and seemed to initially arrive from high latitudes. This negative storm can be attributed to the composition changes driven by storm time thermospheric winds, as mentioned above.

The SAMI3/RCM simulation results showed rather good agreement with both ground-based VTEC and SWC satellite VEC results for the first part of the main phase of the storm, when the PPEF was the principal driver. However, during the second part of the storm, when the ionospheric effects seemed to be driven by a combination of PPEF and thermospheric winds, the SAMI3/RCM simulations showed less compromise with the data. The largest discrepancy between the data and the model is the absence of the strong positive effect in Asian region from ~2:30 to ~7:30 UT on 23 June in the SAMI3/RCM simulation results. This is clearly evident in Animation S1 in the supporting information and in the topside results (Figures 2–5). The reasons for this disagreement are not entirely clear at this time. Several factors may be relevant. First, the disturbance dynamo effect is not correctly modeled (Huba et al., 2016) because the empirical HWM14 wind model is used rather than a first-principles model (e.g., TIEGCM) that can better capture equatorward low- to middle-latitude wind patterns caused by auroral heating. The large enhancement in VTEC observed over Australia is ~3 h after the southward turning of the IMF B_z component, and it seemed to arrive from the equatorial region. Moreover, equatorward winds will lift plasma in the Southern Hemisphere leading to an enhancement in the VTEC. Second, Figure 12 shows significant storm time variations in thermospheric neutral mass density, which can affect neutral composition; this is also not captured in the modeling study because the empirical model NRLMSISE00 is used. One of the major modeling improvements planned in the next year is to self-consistently couple SAMI3/RCM to the first-principles thermosphere model GITM (Ridley et al., 2006). This will allow us to capture both prompt penetration and disturbance dynamo electric fields, as well as thermospheric composition changes during magnetic storms.

3. The 22–23 June 2015 provoked a substantial nighttime increase of the VEC and Ne in the topside ionosphere, especially in Northern (summer) Hemisphere. A strong positive storm is seen in the ionospheric Swarm measurements during the nighttime passes in the 23 LT and 01 LT sectors, when the satellites passed over the African and Atlantic sectors. These observations can be better understood while analyzing the data from the ground-based GNSS receivers (Animation S1). This local VEC enhancement first occurred during the first positive phase over North African sector, which was in the presunset-sunset local sector at that time. With the development of the storm, the enhancement remained

unchangeable for the next several hours, and the satellite measurements prove this result. This midlatitude enhancement might have been produced by the thermospheric winds that moved plasma upward along the magnetic field lines.

4. At the recovery phase of the June 2015 storm, we observed occurrence of the negative ionospheric storm, which is in-line with previous observations (e.g., Astafyeva, Zakharenkova, & Foerster, 2015; Bagiya et al., 2011; Yue et al., 2016; Zhong et al., 2016). This strong decrease of the ionospheric parameters with respect to the quiet time values is usually explained by changes in the neutral composition (e.g., Fuller-Rowell, 2011; Fuller-Rowell et al., 1996).
5. Thermospheric response to the 22–23 June 2015 geomagnetic storm was studied by using for the first time the GPS-derived neutral mass density (ρ) data from Swarm satellites. It is important to note that the Swarm constellation allows a unique opportunity to analyze the thermospheric behavior by identical instruments at different altitudes and in different local time regions. In June 2015, the Swarm spacecraft were separated by only 2 h in local time and by ~70 km in orbital height. However, the results from SWC (flying at ~460 km) showed ~50–70% higher ρ values than those from SWB (flying at ~530 km) during both geomagnetically quiet and disturbed conditions and on both dayside and nightside. The observed difference can be due to the altitudinal difference between the two satellites and also and even more because of the difference in local time, as shown above.

The 22–23 June 2015 geomagnetic storm caused quite significant thermospheric effects; during the main phase of the storm, the neutral mass density increased up to 300–500%, which is comparable to the superstorm values (Liu & Lühr, 2005). The strongest storm time changes were observed in the daytime SWC measurements, while the thermospheric storm effects were the least pronounced in the nighttime SWB data. At both altitudes and on both dayside and nightside, we observed hemispheric asymmetry, with higher absolute neutral mass densities in NH (summer hemisphere). In the meantime, the thermospheric storm time effects seemed less asymmetric, with somewhat stronger effects in NH at the recovery phase of the storm. Overall, we find a good agreement with previous observations of the thermospheric storm time effects observed by using the CHAMP and Gravity Recovery and Climate Experiment satellites (e.g., Astafyeva, Zakharenkova & Doornbos, 2015; Balan et al., 2011, 2012; Liu & Lühr, 2005). Thus, the new recent release of this new data set in addition to already available magnetic and ionospheric data from a constellation of the three satellites makes the Swarm mission more powerful tool for the study of the near-space environment.

Acknowledgments
We thank the NASA/GSFC's Space Physics Data Facility's OMNIWeb service for the data of the interplanetary and geophysical parameters, and the European Space Agency (ESA) EarthNet service (http://earth.esa.int/swarm) for the data from the Swarm constellation. The Swarm thermosphere density data processing is supported by the ESA through the Swarm Data Innovation and Science Cluster (DISC). We acknowledge the use of the raw GPS and GLONASS data provided by the following international and regional networks of GPS/GNSS receivers: IGS (ftp://cddis.gsfc.nasa.gov), UNAVCO (ftp://data-out.unavco.org), CORS (ftp://geodesy.noaa.gov), SOPAC (ftp://garner.ucsd.edu), EPN (ftp://olggps.oeaw.ac.at), BKGE (ftp://igs.bkg.bund.de/euref/obs), IGN (ftp://rgpdata.ign.fr), SWEPOS (swepos.lantmateriet.se), FGI-FinnRef (euref-fin.fgi.fi), NOANET (www.gein.noa.gr), Natural Resources Canada (webapp.geod.nrcan.gc.ca), INEGI (ftp://geodesia.inegi.org.mx), RBMC (ftp://geoftp.ibge.gov.br/RBMC/), and Geoscience Australia (ftp://ga.gov.au). We thank S. Sazykin (William Marsh Rice University) for helpful discussions regarding the RCM model. The results of the SAMI3/RCM simulations can be obtained on demand from J. Huba (huba@nrl.navy.mil). E. A. and I. Z. thank the European Research Council (ERC) for the support (grant agreement 307998). J. D. H. was supported by the NRL Base Funds and NASA.

References

Afraimovich, E. L., Astafyeva, E. I., Demyanov, V. V., Edemskiy, I. K., Gavrilyuk, N. S., Ishin, A. B., … Zhivetiev, I. V. (2013). A review of GPS/GLONASS studies of the ionospheric response to natural and anthropogenic processes and phenomena. *Journal of Space Weather and Space Climate*, *3*, A27. https://doi.org/10.1051/swsc2013049

Afraimovich, E. L., Astafyeva, E. I., Kosogorov, E. A., & Yasyukevich, Y. V. (2011). The mid-latitude field-aligned disturbances and their effects on differential GPS and VLBI. *Advances in Space Research*, *47*(10), 1804–1813. https://doi.org/10.1016/j.asr.2010.06.030

Astafyeva, E., Yasukevich, Y., Maksikov, A., & Zhivetiev, I. (2014). Geomagnetic storms, super-storms and their impact on GPS-based navigation. *Space Weather*, *12*, 508–525, https://doi.org/10.1002/SW001072

Astafyeva, E., Zakharenkova, I., & Alken, P. (2016). Prompt penetration electric fields and the extreme topside ionospheric response to the 22–23 June 2015 geomagnetic storm as seen by the Swarm constellation. *Earth, Planets and Space*, *68*(1), 152. https://doi.org/10.1186/s40623-016-0526-x

Astafyeva, E., Zakharenkova, I., & Doornbos, E. (2015). Opposite hemispheric asymmetries during the ionospheric storm of 29–31 August 2004. *Journal of Geophysical Research*, *120*(1), 697–714. https://doi.org/10.1002/2014JA020710

Astafyeva, E., Zakharenkova, I., & Foerster, M. (2015). Ionospheric response to the 2015 St. Patrick's Day storm: A global multi-instrumental overview. *Journal of Geophysical Research*, *120*(10), 9023–9037. https://doi.org/10.1002/2015JA021629

Astafyeva, E. I., Afraimovich, E. L., & Kosogorov, E. A. (2007). Dynamics of total electron content distribution during strong geomagnetic storms. *Advances in Space Research*, *39*(8), 1313–1317. https://doi.org/10.1016/j.asr.2007.03.006

Bagiya, M. S., Iyer, K. N., Joshi, H. P., Thampi, S. V., Tsugawa, T., Ravindran, S., … Pathan, B. M. (2011). Low-latitude ionospheric thermospheric response to storm time electrodynamical coupling between high and low latitudes. *Journal of Geophysical Research*, *116*(A1), A01303. https://doi.org/10.1029/2010JA015845

Balan, N., Liu, J. Y., Otsuka, Y., Tulasi Ram, S., & Lühr, H. (2012). Ionospheric and thermospheric storms at equatorial latitudes observed by CHAMP, ROCSAT, and DMSP. *Journal of Geophysical Research*, *117*(A1), A01313. https://doi.org/10.1029/2011JA016903

Balan, N., Yamamoto, M., Liu, J. Y., Liu, H., & Lühr, H. (2011). New aspects of thermospheric and ionospheric storms revealed by CHAMP. *Journal of Geophysical Research*, *116*(A7), A07305. https://doi.org/10.1029/2010JA016399

Basu, S., Basu, S., Makela, J. J., MacKenzie, E., Doherty, P., Wright, J. W., … Coster, A. J. (2008). Large magnetic storm-induced nighttime ionospheric flows at mid-latitudes and their impacts on GPS-based navigation systems. *Journal of Geophysical Research*, *113*(A3), A00A06. https://doi.org/10.1029/2008JA013076

Blanc, M., & Richmond, A. D. (1980). The ionospheric disturbance dynamo. *Journal of Geophysical Research*, *85*(A4), 1669–1686. https://doi.org/10.1029/JA085iA04p01669

Chamberlin, P. C., Woods, T. N., & Eparvier, F. G. (2007). Flare Irradiance Spectral Model (FISM): Daily component algorithms and results. *Space Weather*, *5*, S07005. https://doi.org/10.1029/2007SW000316

Clausen, L. B. N., Milan, S. E., & Grocott, A. (2014). Thermospheric density perturbations in response to substorms. *Journal of Geophysical Research: Space Physics*, *119*(6), 4441–4455. https://doi.org/10.1002/2014JA019837

Drob, D. P., Emmert, J. T., Meriwether, J. W., Makela, J. J., Doornbos, E., Conde, M., … Klenzing, J. H. (2015). An update to the horizontal wind model (HWM): The quiet time thermosphere. *Earth and Space Science*, *2*(7), 301–319. https://doi.org/10.1002/2014EA000089

Fejer, B. G., Jensen, J. W., Kikuchi, T., Abdu, M. A., & Chau, J. L. (2007). Equatorial ionospheric electric fields during the November 2004 magnetic storm. *Journal of Geophysical Research*, *112*(A10), A10304. https://doi.org/10.1029/2007JA012376

Foster, J. C., & Coster, A. J. (2007). Conjugate localized enhancement of total electron content at low latitudes in the American sector. *Journal of Atmospheric and Solar-Terrestrial Physics*, *69*(10–11), 1241–1252. https://doi.org/10.1016/j.jastp.2006.09.012

Foster, J. C., & Rideout, W. (2005). Midlatitude TEC enhancements during the October 2003 superstorm. *Geophysical Research Letters*, *32*(12), L12S04. https://doi.org/10.1029/2004GL02719

Fuller-Rowell, T. J. (2011). Storm-time response of the thermosphere-ionosphere system. In M. A. Abdu, D. Pancheva, & A. Bhattacharyya (Eds.), *Aeronomy of the Earth's Atmosphere and Ionosphere*, *IAGA Spec. Sopron Book Ser*, (Vol. 2, chapt. 32, pp. 419–435). Dordrecht, Netherlands: Springer. https://doi.org/10.1007/%20978-94-007-0326-1

Fuller-Rowell, T. J., Codrescu, M. V., Rishbeth, H., Moffett, R. J., & Quegan, S. (1996). On the seasonal response of the thermosphere and ionosphere to geomagnetic storms. *Journal of Geophysical Research*, *101*(A2), 2343–2353. https://doi.org/10.1029/95JA01614

Fuller-Rowell, T. J., & Rees, D. (1981). A three-dimensional, time-dependent simulation of the global dynamical response of the thermosphere to a geomagnetic substorm. *Journal of Atmospheric and Terrestrial Physics*, *43*(7), 701–721. https://doi.org/10.1016/0021-9169(81)90142-2

Gonzalez, W. D., Joselyn, J. A., Kamide, Y., Kroehl, H. W., Rostoker, G., Tsurutani, B. T., & Vasyliunas, V. M. (1994). What is a geomagnetic storm? *Journal of Geophysical Research*, *99*(A4), 5771–5792. https://doi.org/10.1029/93JA02867

Hilmer, R. V., & Voigt, G. H. (1995). A magnetospheric magnetic field model with current systems driven by independent physical parameters. *Journal of Geophysical Research*, *100*(A4), 5613. https://doi.org/10.1029/94JA03139

Huang, C.-S., Foster, J. C., & Kelley, M. C. (2005). Long-duration penetration of the interplanetary electric field to the low-latitude ionosphere during the main phase of magnetic storms. *Journal of Geophysical Research*, *110*(A11), A11309. https://doi.org/10.1029/2005JA011202

Huba, J. D., & Joyce, G. (2010). Global modeling of equatorial plasma bubbles. *Geophysical Research Letters*, *37*(17), L17104. https://doi.org/10.1029/2010GL044281

Huba, J. D., Joyce, G., & Fedder, J. A. (2000). SAMI2 is Another Model of the Ionosphere (SAMI2): A new low-latitude ionosphere model. *Journal of Geophysical Research*, *105*(A10), 23,035–23,053. https://doi.org/10.1029/2000JA000035

Huba, J. D., Joyce, G., Sazykin, S., Wolf, R., & Spiro, R. (2005). Simulation study of penetration electric field effects on the low- to mid-latitude ionosphere. *Geophysical Research Letters*, *32*(23), L23101. https://doi.org/10.1029/2005GL024162

Huba, J. D., & Sazykin, S. (2014). Storm time ionosphere and plasmasphere structuring: SAMI3-RCM simulation of the 31 March 2001 geomagnetic storm. *Geophysical Research Letters*, *41*(23), 8208–8214. https://doi.org/10.1002/2014GL062110

Huba, J. D., Sazykin, S., & Coster, A. (2016). SAMI3-RCM simulation of the 17 March 2015 geomagnetic storm. *Journal of Geophysical Research: Space Physics*, *122*, https://doi.org/10.1002/2016JA023341, 1246–1257.

Kelly, M. A., Comberiate, J. M., Miller, E. S., & Paxton, L. J. (2014). Progress toward forecasting of space weather effects on UHF SATCOM after operation anaconda. *Space Weather*, *12*, 601–611. https://doi.org/10.1002/2014SW001081

Kikuchi, T., & Hashimoto, K. (2016). Transmission o f the electric fields to the low latitude ionosphere in the magnetosphere-ionosphere current circuit. *Geoscience Letters*, *3*(1), 1–11. https://doi.org/10.1186/s40562-016-0035-6

Lei, J., Wang, W., Burns, A. G., Solomon, S. C., Richmond, A. D., Wiltberger, M., … Reinisch, B. W. (2008). Observations and simulations of the ionospheric and thermospheric response to the December 2006 geomagnetic storm: Initial phase. *Journal of Geophysical Research*, *113*(A1), A01314. https://doi.org/10.1029/2007JA012807

Lei, J., Wang, W., Burns, A. G., Yue, X., Dou, X., Luan, X., … Liu, Y. C.-M. (2014). New aspects of the ionospheric response to the October 2003 superstorms from multiple-satellite observations. *Journal of Geophysical Research: Space Physics*, *119*(3), 2298–2317. https://doi.org/10.1002/2013JA019575

Liu, H., & Lühr, H. (2005). Strong disturbance of the upper thermospheric density due to magnetic storms: CHAMP observations. *Journal of Geophysical Research*, *110*(A9), A09S29. https://doi.org/10.1029/2004JA010908

Liu, J., Liu, L., Nakamura, T., Zhao, B., Ning, B., & Yoshikawa, A. (2014). A case study of ionospheric storm effects during long-lasting southward IMF B_z-driven geomagnetic storm. *Journal of Geophysical Research*, *119*(9), 7716–7731. https://doi.org/10.1002/2014JA020273

Liu, J.-Y., Lin, C. H., Chen, Y. I., Lin, Y. C., Fang, T. W., Chen, C. H., … Hwang, J. J. (2006). Solar flare signatures of the ionospheric GPS total electron content. *Journal of Geophysical Research*, *111*(A5), A05308. https://doi.org/10.1029/2005JA011306

Liu, Y. D., Hu, H., Wang, R., Yang, Z., Zhu, B., Liu, Y. A., … Richardson, J. D. (2015). Plasma and magnetic field characteristics of solar coronal mass ejections in relation to geomagnetic storm intensity and variability. *The Astrophysical Journal Letters*, *809*(2), L34. https://doi.org/10.1088/2041-8205/809/2/L34

Mannucci, A. J., Wilson, B. D., Yuan, D. N., Ho, C. H., Lindqwister, U. J., & Runge, T. F. (1998). A global mapping technique for GPS-derived ionospheric total electron content measurements. *Radio Science*, *33*(3), 565–582. https://doi.org/10.1029/97RS02707

Maruyama, N., Richmond, A. D., Fuller-Rowell, T. J., Codrescu, M. V., Sazykin, S., Toffoletto, F. R., … Millward, G. H. (2005). Interaction between direct penetration and disturbance dynamo electric fields in the storm-time equatorial ionosphere. *Geophysical Research Letters*, *32*(17), L17105. https://doi.org/10.1029/2005GL023763

Nayak, C., Tsai, L.-C., Su, S.-Y., Galkin, I. A., Tan, A. T. K., Nofri, E., & Jamjareegulgarn, P. (2016). Peculiar features of the low-latitude and mid-latitude ionospheric response to the St. Patrick's Day geomagnetic storm of 17 March 2015. *Journal of Geophysical Research: Space Physics*, *121*(8), 7941–7960. https://doi.org/10.1002/2016JA022489

Olsen, N., Friis-Christensen, E., Floberghagen, R., Alken, P., Beggan, C. D., Chulliat, A., … Visser, P. N. (2013). The Swarm Satellite Constellation Application and Research Facility (SCARF) and Swarm data products. *Earth, Planets and Space*, *65*(11), 1189–1200. https://doi.org/10.5047/eps.2013.07.001

Picone, J., Hedin, A., Drob, D., & Aikin, A. (2002). NRLMSISE-00 empirical model of the atmosphere: Statistical comparisons and scientific issues. *Journal of Geophysical Research*, *107*(A12), 1468. https://doi.org/10.1029/2002JA009430, SIA 15-1, SIA 15-16.

Richmond, A. (1995). Ionospheric electrodynamics using magnetic apex coordinates. *Journal of Geomagnetism and Geoelectricity*, *47*(2), 191–212. https://doi.org/10.5636/jgg.47.191

Ridley, A., Deng, Y., & Toth, G. (2006). The global ionosphere-thermosphere model. *Journal of Atmospheric and Solar-Terrestrial Physics*, *68*(8), 839–864. https://doi.org/10.1016/j.jastp.2006.01.008

Ritter, P., Luhr, H., & Doornbos, E. (2010). Substorm-related thermospheric density and wind disturbances derived from CHAMP observations. *Annales Geophysicae*, *28*(6), 1207–1220. https://doi.org/10.5194/angeo-28-1207-2010

Sastri, J. H., Kamide, Y., & Yumoto, K. (2003). Signatures for magnetospheric substorms in the geomagnetic field of dayside equatorial region: Origin of the ionospheric component. *Journal of Geophysical Research*, *108*(A10), 1375. https://doi.org/10.1029/2003JA009962

Sazykin, S., Wolf, R. A., Spiro, R. W., Gombosi, T. I., De Zeeuw, D. L., & Thomsen, M. F. (2002). Interchange instability in the inner magnetosphere associated with geosynchronous particle flux decreases. *Geophysical Research Letters*, *29*(10), 1148. https://doi.org/10.1029/2001GL014416, 88-1, 88-4

Schunk, R. W., Zhu, L., Sojka, J. J., & Bowline, M. D. (1997). Ionospheric response to an auroral substorm. *Geophysical Research Letters*, *24*(16), 1979–1982. https://doi.org/10.1029/97GL01252

Siemes, C., de Teixeira da Encarnação, J., Doornbos, E., van den IJssel, J., Kraus, J., Pereštý, R., … Olsen, P. E. H. (2016). Swarm accelerometer data processing from raw accelerations to thermospheric neutral densities. *Earth, Planets and Space*, *68*(1), 92. https://doi.org/10.1186/s40623-016-0474-5

Sobral, J. H. A., Abdu, M. A., Gonzalez, W. D., Tsurutani, B. T., Batista, I. S., & Clua de Gonzalez, A. L. (1997). Effects of intense storms and substorms on the equatorial ionosphere/thermosphere system in the American sector from ground-based and satellite data. *Journal of Geophysical Research*, *102*(A7), 14,305–14,313. https://doi.org/10.1029/97JA00576

Toffoletto, F., Sazykin, S., Spiro, R. W., & Wolf, R. A. (2003). Inner magnetospheric modeling with the Rice Convection Model. *Space Science Reviews*, *107*(1/2), 175–196. https://doi.org/10.1023/A:1025532008047

Tsugawa, T., Saito, A., Otsuka, Y., & Yamamoto, M. (2003). Damping of large-scale traveling ionospheric disturbances detected with GPS networks during the geomagnetic storm. *Journal of Geophysical Research*, *108*(A3), 1127. https://doi.org/10.1029/2002JA009433

Tsurutani, B., Mannucci, A., Iijima, B., Abdu, M. A., Sobral, J. H. A., Gonzalez, W., … Tsuda, T. (2004). Global dayside ionospheric uplift and enhancement associated with interplanetary electric fields. *Journal of Geophysical Research*, *109*, A08302, https://doi.org/10.1029/2003JA010342

van den IJssel, J., & Visser, P. (2007). Performance of GPS-based accelerometry: CHAMP and GRACE. *Advances in Space Research*, *39*(10), 1597–1603. https://doi.org/10.1016/j.asr.2006.12.027

van den IJssel, J. A. A. (2014). GPS-based precise orbit determination and accelerometry for low flying satellites, doctoral thesis, TU Delft. https://doi.org/10.4233/uuid:9aabcd0f-d984-4d7f-8567-677689e07c85

Verkhoglyadova, O. P., Tsurutani, B. T., Mannucci, A. J., Mlynczak, M. G., Hunt, L. A., & Runge, T. (2013). Variability of ionospheric TEC during solar and geomagnetic minima (2008 and 2009): External high speed stream drivers. *Annales Geophysicae*, *31*(2), 263–276. https://doi.org/10.5194/angeo-31-263-2013

Verkhoglyadova, O. P., Tsurutani, B. T., Mannucci, A. J., Saito, A., Araki, T., Anderson, D., … Sobral, J. H. A. (2008). Simulation of PPEF effects in dayside low-latitude ionosphere for the October 30, 2003 superstorm. In P. Kintner, et al. (Eds.), *Mid-Latitude Ionosphere Dynamics and Disturbances*. *Geophysical Monograph Series* (Vol. 181, pp. 169–171).Washington, DC: American Geophysical Union. http://doi.wiley.com/10.1029/181GM16

Wolf, R. A., Spiro, R. W., & Rich, F. J. (1991). Extension of convection modeling into the high-latitude ionosphere: Some theoretical difficulties. *Journal of Atmospheric and Terrestrial Physics*, *53*(9), 817–829. https://doi.org/10.1016/0021-9169(91)90096-P

Yue, X., Wang, W., Lei, J., Burns, A., Zhang, Y., Wan, W., … Schreiner, W. S. (2016). Long-lasting negative ionospheric storm effects in low and middle latitudes during the recovery phase of the 17 March 2013 geomagnetic storm. *Journal of Geophysical Research: Space Physics*, *121*(9), 9234–9249. https://doi.org/10.1002/2016JA022984

Zakharenkova, I., & Astafyeva, E. (2015). Topside ionospheric irregularities as seen from multi-satellite observations. *Journal of Geophysical Research: Space Physics*, *120*(1), 807–824. https://doi.org/10.1002/2014JA020330

Zakharenkova, I., Astafyeva, E., & Cherniak, I. (2016). GPS and GLONASS observations of traveling ionospheric disturbances during the 2015 St. Patrick's Day storm. *Journal of Geophysical Research: Space Physics*, *121*(12), 12,138–12,156, https://doi.org/10.1002/2016JA023332

Zhong, J., Wang, W., Yue, X., Burns, A. G., Dou, X., & Lei, J. (2016). Long-duration depletion in the topside ionospheric total electron content during the recovery phase of the March 2015 strong storm. *Journal of Geophysical Research: Space Physics*, *121*(5), 4733–4747. https://doi.org/10.1002/2016JA022469